



1 **High atmospheric oxidation capacity drives wintertime nitrate pollution in the eastern**

2 **Yangtze River Delta of China**

3

4 Han Zang¹, Yue Zhao^{1,*}, Juntao Huo², Qianbiao Zhao², Qingyan Fu², Yusen Duan^{2,*}, Jingyuan Shao³,
5 Cheng Huang⁴, Jingyu An⁴, Likun Xue⁵, Ziyue Li¹, Chenxi Li¹, Huayun Xiao¹

6

7 ¹School of Environmental Science and Engineering, Shanghai Jiao Tong University, Shanghai, 200240,
8 China

9 ²Shanghai Environmental Monitoring Center, Shanghai 200235, China

10 ³College of Flight Technology, Civil Aviation University of China, Tianjin 300300, China

11 ⁴Shanghai Academy of Environmental Sciences, Shanghai 200233, China

12 ⁵Environment Research Institute, Shandong University, Qingdao, Shandong, 266237, China

13

14 *Correspondence: Yue Zhao (yuezhao20@sjtu.edu.cn); Yusen Duan (duanys@yeah.net)

15



16 **Abstract**

17 Nitrate aerosol plays an increasingly important role in wintertime haze pollution in China. Despite
18 intensive research on the wintertime nitrate chemistry in recent years, quantitative constraints on
19 the formation mechanisms of nitrate aerosol in the Yangtze River Delta (YRD), one of the most
20 developed and densely populated regions in eastern China, remain inadequate. In this study, we
21 identify the major nitrate formation pathways and their key controlling factors during the winter
22 haze pollution period in the eastern YRD using two-year (2018-2019) field observations and
23 detailed observation-constrained model simulations. We find that the high atmospheric oxidation
24 capacity, coupled with high aerosol liquid water content (ALWC), made both the heterogeneous
25 hydrolysis of dinitrogen pentoxide (N_2O_5) and the gas-phase OH oxidation of nitrogen dioxide (NO_2)
26 important pathways for wintertime nitrate formation in this region, with contribution percentages of
27 69% and 29% in urban areas and 63% and 35% in suburban areas, respectively. We further find that
28 the gas-to-particle partitioning of nitric acid (HNO_3) was very efficient so that the rate-determining
29 step in the overall formation process of nitrate aerosol was the oxidation of NO_x to HNO_3 through
30 both heterogeneous and gas-phase processes. The atmospheric oxidation capacity (i.e., the
31 availability of O_3 and OH radicals) was the key factor controlling the production rate of HNO_3 from
32 both processes. During the COVID-19 lockdown (January-February 2020), the enhanced
33 atmospheric oxidation capacity greatly promoted the oxidation of NO_x to nitrate and hence
34 weakened the response of nitrate aerosol to the emission reductions in urban areas. Our study sheds
35 light on the detailed formation mechanisms of wintertime nitrate aerosol in the eastern YRD and
36 highlights the demand for the synergetic regulation of atmospheric oxidation capacity and NO_x
37 emissions to mitigate wintertime nitrate and haze pollution in eastern China.
38



39 1. Introduction

40 Atmospheric fine particulate matter (PM_{2.5}) has profound impacts on air quality, climate, and public
41 health (Huang et al., 2014; Wang et al., 2014; Lelieveld et al., 2015; von Schneidemesser et al.,
42 2015). Over the past decades, China has encountered severe PM_{2.5} pollution due to the rapid
43 urbanization and industrialization (Huang et al., 2014; Zhang and Cao, 2015; Tao et al., 2017; Peng
44 et al., 2021). To tackle severe air pollution, Chinese government has implemented active clean air
45 policies such as the “Action Plan for Air Pollution Prevention and Control” in recent years. As a
46 result, anthropogenic emissions of major air pollutants such as sulfur dioxide (SO₂), nitrogen oxides
47 (NO_x), and primary PM have declined dramatically and the nationwide PM_{2.5} air quality have
48 improved significantly (Shao et al., 2018; Zheng et al., 2018; Ding et al., 2019; Zhang et al., 2019).
49 In addition, with the emission reduction of primary PM, secondary aerosol has become the most
50 important component of PM_{2.5} (Shao et al., 2018; Ding et al., 2019; Peng et al., 2021).

51

52 Secondary inorganic aerosol consisting mainly of nitrate, sulfate, and ammonium (SNA),
53 contributed to 30-60% of the PM_{2.5} mass in China (Hua et al., 2015; Tao et al., 2017; Ye et al., 2017;
54 Wang et al., 2018; Fu et al., 2020; Lin et al., 2020). During the pollution episodes, the proportion of
55 SNA to PM_{2.5} could exceed 50% (Tao et al., 2017; Liu et al., 2020; Peng et al., 2021). Before 2013,
56 sulfate was often found to be the most abundant component of PM_{2.5} in Chinese cities (Zhao et al.,
57 2013; Huang et al., 2014; Kong et al., 2014; Xie et al., 2015; Tao et al., 2017). However, with the
58 implementation of stringent clean air policies, anthropogenic emissions of SO₂ in China had
59 dropped by 59% from 2013 to 2017, while NO_x emissions decreased only by 21% during the same
60 period (Zheng et al., 2018). Consequently, sulfate aerosol concentration has decreased dramatically
61 nationwide since 2013, but wintertime nitrate concentration has not decreased much (Ding et al.,
62 2019; Li et al., 2019a; Xu et al., 2019; Fu et al., 2020; Wang et al., 2020b); nitrate has become an
63 increasingly important component of PM_{2.5} in most regions of China during winter (Ye et al., 2017;
64 Yun et al., 2018; Li et al., 2019a; Xu et al., 2019; Chen et al., 2020; Fu et al., 2020; Kong et al.,
65 2020; Lin et al., 2020; Xie et al., 2020; Zhai et al., 2021; Zhang et al., 2021). The high loading of
66 nitrate has been considered playing an important role in winter haze pollution (Wen et al., 2015;
67 Sun et al., 2018). Therefore, identifying the major nitrate formation pathways and their controlling
68 factors during haze events is of great importance for developing effective particulate pollution
69 mitigation policies in China.

70

71 In polluted regions, the nitrate aerosol arises mainly from two pathways: (1) the gas-phase oxidation
72 of nitrogen dioxide (NO₂) by OH radicals producing nitric acid (HNO₃) (Calvert and Stockwell,
73 1983) and (2) the heterogeneous hydrolysis of dinitrogen pentoxide (N₂O₅) that was produced from
74 the reaction of NO₂ with nitrate (NO₃) radicals, on aqueous aerosols (Bertram and Thornton, 2009;
75 Bertram et al., 2009; Wagner et al., 2013; McDuffie et al., 2019). The gas-phase OH + NO₂ pathway
76 primarily occurs during the daytime and is mainly influenced by the atmospheric oxidation capacity
77 despite the NO₂ concentration (Chen et al., 2020; Fu et al., 2020). The heterogeneous formation of
78 nitrate via N₂O₅ hydrolysis is greatly affected by aerosol liquid water content (ALWC) and the



79 production of N_2O_5 (Alexander et al., 2020; Lin et al., 2020; Wang et al., 2020b). As a result, this
80 heterogeneous pathway is generally weak during the daytime because of the fast photolysis of NO_3
81 radicals or titration by NO (Wayne et al., 1991; Brown and Stutz, 2012), which inhibit N_2O_5
82 production. However, it could be the dominant pathway for nitrate formation during the nighttime
83 (Wang et al., 2017; McDuffie et al., 2019), where N_2O_5 can be produced more efficiently and its
84 hydrolysis is favored by the high relative humidity (or ALWC).

85
86 There have been a number of field studies on the pollution characteristics and formation
87 mechanisms of nitrate aerosol during haze events in China over the past decades (Tao et al., 2016;
88 Li et al., 2018; Sun et al., 2018; Wen et al., 2018; Ding et al., 2019; Ye et al., 2019; Chen et al., 2020;
89 Fu et al., 2020; Lin et al., 2020; Wang et al., 2020b; Zhao et al., 2020a; Chan et al., 2021). However,
90 most of these studies were carried out in the North China Plain (NCP) (Li et al., 2018; Wen et al.,
91 2018; Chen et al., 2020; Fu et al., 2020; Wang et al., 2020b; Chan et al., 2021). Earlier studies
92 suggested that the nitrate formation during the pollution episodes in this region was mainly
93 attributed to the heterogeneous hydrolysis of N_2O_5 (Su et al., 2017; Wang et al., 2017; He et al.,
94 2018; Li et al., 2018). However, recent studies showed that the gas-phase $\text{OH} + \text{NO}_2$ process has
95 become more important, and sometimes this process was even the dominant pathway for nitrate
96 formation (Chen et al., 2020; Fu et al., 2020). The Yangtze River Delta (YRD) in eastern China is
97 one of the most developed regions in China (Ding et al., 2013). The wintertime O_3 concentration is
98 relatively high in this region, with an average of ~ 20 ppb, and sometimes could even reach 75 ppb
99 (Li et al., 2019c; Ye et al., 2019; Zhao et al., 2020a), which is significantly higher than that (average:
100 6–16 ppb) in the NCP region (Li et al., 2019a; Duan et al., 2020; Liu et al., 2020). Furthermore, the
101 relative humidity (RH) in this region is also high, with the average winter RH ranging from 63% to
102 71% (Tao et al., 2016; Shen et al., 2020; Yu et al., 2020b), which was also significantly higher than
103 the average RH (20–40%) in the NCP region (Fang et al., 2019; Li et al., 2019a; Huang et al., 2020;
104 Xie et al., 2020). The high atmospheric oxidation capacity, coupled with the high RH that led to
105 high ALWC, would favor the production of secondary aerosol (Peng et al., 2021).

106
107 Haze pollution events frequently occurred in the YRD during winter (Hua et al., 2015; Sun et al.,
108 2018; Ding et al., 2019). Although there have been many studies on the pollution characteristics of
109 nitrate and $\text{PM}_{2.5}$ in this region (Tao et al., 2016; Sun et al., 2018; Chen et al., 2019; Ding et al.,
110 2019; Ye et al., 2019; Lin et al., 2020; Shen et al., 2020), only a few studies have focused on the
111 nitrate formation mechanisms. It has been reported that the heterogeneous hydrolysis of N_2O_5
112 contributed dominantly to nitrate formation in the western YRD (Sun et al., 2018), and its
113 production rate could be 5 times higher than that of the gas-phase $\text{OH} + \text{NO}_2$ process during severe
114 haze pollution events (Lin et al., 2020). In contrast, some other studies have qualitatively pointed
115 out that the gas-phase $\text{OH} + \text{NO}_2$ reaction was an important formation pathway of nitrate in the
116 eastern YRD, though the heterogeneous hydrolysis of N_2O_5 during the nighttime also contributed
117 (Ye et al., 2019; Zhao et al., 2020a). Overall, quantitative constraints on the detailed formation
118 mechanisms of wintertime nitrate aerosol in the YRD region remain limited. The relative



119 contribution of different nitrate formation pathways and their controlling factors are still unclear.

120

121 In this study, we conducted hourly measurements of nitrate and associated particulate and gaseous
122 air pollutants at an urban site and a regional site in the eastern YRD during winter in 2018 and 2019,
123 aiming to clarify the nitrate formation mechanisms during winter. An observation-constrained box
124 model using the detailed Master Chemical Mechanism (MCM v3.3.1) updated with the state-of-the-
125 art heterogeneous chemistry of N_2O_5 , NO_2 , and particulate nitrate was employed to quantitatively
126 identify the major reaction pathways and key controlling factors for wintertime nitrate aerosol
127 formation in this region. This study will help to understand the nitrate aerosol chemistry in the
128 eastern YRD and develop effective strategies to mitigate secondary aerosol pollution in this densely
129 populated region.

130

131 2. Materials and methods

132 2.1 Observation sites and instrumentation

133 $\text{PM}_{2.5}$ and its chemical composition, inorganic gases, volatile organic compounds (VOCs), and
134 meteorological parameters were continuously measured at a regional site (Qingpu) and an urban site
135 (Pudong) in Shanghai from December 1 to February 12 in both 2018 and 2019. The Qingpu site
136 (120.989°E , 31.097°W) is a suburban site (see Fig. 1), located near the Dianshan Lake and
137 surrounded by the residential areas and vegetation, and about 46 km away from the urban Shanghai.
138 Besides, the Qingpu site is located at the junction of Shanghai, Jiangsu, and Zhejiang province and
139 is a typical regional site in the eastern YRD. The instruments at this site were on the rooftop of a 10
140 m tall building. The Pudong site (121.533°E , 31.228°W) is an urban site located near the Century
141 Avenue with heavy traffic, and it is only ~ 3 km from the business center Lujiazui. The instruments
142 at this site were located on the roof of a 20 m tall building. The eastern YRD region is affected by
143 the subtropical monsoon climate, dominated by the northwest and northeast winds in winter.

144

145 The measurements at the two sites were conducted hourly. The $\text{PM}_{2.5}$ mass concentration was
146 measured by a Tapered Element Oscillating Microbalance combined with Filter Dynamic
147 Measurement System (TEOM-FDMS, TEOM 1405-F, Thermo Fisher Scientific, USA.). Water-
148 soluble ions including NO_3^- , SO_4^{2-} , NH_4^+ , Cl^- , Na^+ , Ca^{2+} , and Mg^{2+} were measured using an online
149 Monitor for Aerosol and Gases (MARGA, ADI 2080, Applikon Analytical B.B.Corp., Netherlands).
150 Organic carbon (OC) and elemental carbon (EC) were measured by a semi-continuous OC/EC
151 analyzer (Model 4, Sunset Laboratory Inc., USA), and a denuder was installed before analyzer to
152 avoid the disturbance of organic vapors. The surface area and volume concentrations of aerosol
153 particles were measured using a scanning mobility particle sizer (SMPS, TSI, USA, which consists
154 of a 3080 electrostatic classifier, a 3081A differential mobility analyzer, and a 3787 condensation
155 particle counter) and an aerodynamic particle sizer (APS 3321, TSI, USA). The combination of
156 SMPS and APS was able to cover the particle size range from 13.6 nm to 10 μm . Considering that
157 the Pudong sampling site lacks the data of aerosol volume and surface area concentrations, we
158 performed a linear fit between the aerosol surface/volume and $\text{PM}_{2.5}$ mass concentration at the



159 Qingpu site (see Figure S1 in the supplement), and predicted the values for the Pudong site based
160 on such a linear fit and the measured PM_{2.5} mass concentration. The surface/volume concentrations
161 of dry aerosol particles measured by SMPS and APS were corrected to the ambient RH based on an
162 empirical composition-kappa function and the kappa-Köhler function (see details in Section S1 of
163 the Supplement). The O₃, NO_x, and SO₂ were measured by an Ozone, NO_x, and SO₂ analyzer (Model
164 49i, 42i, and 43i, Thermo Fisher Scientific, USA), respectively. A total of 56 VOCs were measured
165 using gas chromatography equipped with a flame ionization detector (GC-FID, Chromatotec
166 A11000/A21022 at the Qingpu site and PerkinElmer Clarus 580 at the Pudong site). Meteorological
167 parameters including temperature, RH, pressure, wind speed and direction were measured by a
168 meteorological transducer (WXT520, Vaisala Ltd., Finland).

169

170 2.2 Estimation of aerosol liquid water content and pH

171 The ISORROPIA-II thermodynamic model was used to calculate aerosol pH and ALWC
172 (Fountoukis and Nenes, 2007). The water-soluble inorganic ion concentrations, along with RH and
173 temperature, were used as the model input. The model was run in the forward mode, which would
174 give a more accurate estimation of aerosol pH than using the reverse mode with only particulate
175 inorganic ions as the model input (Guo et al., 2015; Hennigan et al., 2015). Besides, considering the
176 relatively high RH in eastern YRD, we selected the metastable state for aerosol in this study.
177 ISORROPIA-II calculated the equilibrium concentrations of particle hydronium ions (H_{air}⁺, μg m⁻³)
178 and ALWC (μg m⁻³) in per air volume. Then the aerosol pH can be derived by the following equation:

$$179 \quad \text{pH} = -\log_{10}(\text{H}_{\text{aq}}^+) = -\log_{10} \frac{1000\text{H}_{\text{air}}^+}{\text{ALWC}} \quad (1)$$

180 Where H_{aq}⁺ is the concentration of hydronium ions in aqueous aerosol (mol L⁻¹). It should be
181 mentioned that when the RH was extremely high (> 95%), a slight deviation in measured RH would
182 cause significant uncertainty in the estimation of ALWC. Therefore, we only considered the data
183 with the RH below 95% in the further analysis.

184

185 2.3 Observation-constrained model simulation

186 The Framework for 0-D Atmospheric Modeling (F0AM v3.1) (Wolfe et al., 2016) employing the
187 MCM v3.3.1 (Jenkin et al., 2015) was used to simulate the formation of nitrate in the pollution
188 events during the whole observation period. Figure 2 summarizes the formation pathways of HNO₃
189 in the atmosphere (Alexander et al., 2020; Chan et al., 2021). In the model, we considered the
190 reaction pathways including heterogeneous hydrolysis of N₂O₅ (R3) and NO₂ (R8), gas-phase OH
191 + NO₂ (R7), NO₃ radical oxidation of VOCs (R5), and reaction of NO with hydroperoxy (HO₂)
192 radicals (R2), which together contributed to 88% of HNO₃ formation in the global troposphere
193 (Alexander et al., 2020). The model did not include the hydrolysis of NO₃ radicals and organic
194 nitrate (R1, R4, and R6), as well as the reaction of NO₂ with halogen oxide species (R9). However,
195 these pathways only had a small contribution to the production of HNO₃ (Alexander et al., 2020).
196 Therefore, they would not significantly affect the model results in this study.

197



198 The default MCMv3.3.1 does not consider the heterogeneous hydrolysis of N_2O_5 in detail and the
199 heterogeneous production of nitrous acid (HONO), an important precursor of OH radicals in the
200 polluted atmosphere. Therefore, we parameterized these processes in the model based on recent
201 advances in these processes. The rate of the heterogeneous hydrolysis of N_2O_5 on aqueous aerosols
202 (k_3) could be calculated by eq. 2 when ignoring the gas-phase diffusion limitation:

$$203 \quad k_3 = \frac{\gamma N_2O_5 \cdot c \cdot S_a}{4} \quad (2)$$

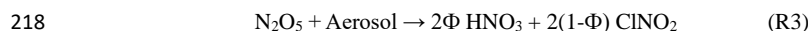
204 where γN_2O_5 is the uptake coefficient of N_2O_5 , defined as the probability of removal of N_2O_5 per
205 collision with the wet aerosol surface; c is the mean molecular speed of N_2O_5 ; S_a is the measured
206 aerosol surface area concentration. In this study, we employed an observation-based empirical
207 parameterization of γN_2O_5 , which provided a reasonable representation of the $PM_{2.5}$ reactivity
208 toward N_2O_5 at different Chinese sites, according to a recent study (Yu et al., 2020a):

$$209 \quad \gamma N_2O_5 = \frac{4}{c} \frac{V_a}{S_a} K_H \times 3.0 \times 10^4 \times [H_2O] \times \left(1 - \frac{1}{\left(0.033 \times \frac{[H_2O]}{[NO_3^-]} \right) + 1 + \left(3.4 \times \frac{[Cl^-]}{[NO_3^-]} \right)} \right) \quad (3)$$

210 where V_a is the measured aerosol volume concentration; K_H is the Henry's law coefficient of N_2O_5 ,
211 with a value of 51 M atm^{-1} (Bertram and Thornton, 2009); and $[H_2O]$, $[NO_3^-]$, and $[Cl^-]$ are the
212 molarity of water, nitrate, and chloride in aerosol, respectively.

213

214 The heterogeneous hydrolysis of N_2O_5 on aqueous aerosols could form HNO_3 and/or nitryl chloride
215 ($ClNO_2$) (see R3), with their yields (i.e., the value of Φ , ranging between 0 and 1) depending on the
216 H_2O and Cl^- content in the aerosol (Bertram and Thornton, 2009; Yu et al., 2020a). In this study, the
217 yield of HNO_3 (Φ_{HNO_3}) was estimated from eq. 4 (Bertram and Thornton, 2009; Yu et al., 2020a):



$$219 \quad \Phi_{HNO_3} = 1 - 1 / \left(1 + \frac{[H_2O]}{105 \times [Cl^-]} \right) \quad (4)$$

220

221 Photolysis of HONO was shown to contribute 20-92% of the production of OH radicals during
222 winter haze pollution events in China (Tan et al., 2017; Slater et al., 2020; Xue et al., 2020). Here,
223 on the basis of previous studies (Lee and Schwartz, 1983; Kleffmann et al., 1998; Kurtenbach et al.,
224 2001; Wong et al., 2011; Wong et al., 2013; Han et al., 2016; Ye et al., 2016; Liu et al., 2017; Trinh
225 et al., 2017; Romer et al., 2018; Zare et al., 2018; Liu et al., 2019; Wang et al., 2020a; Xue et al.,
226 2020), we parameterized the major heterogeneous production pathways of HONO and its dry
227 deposition to estimate the HONO budget during the pollution episodes. The added mechanisms are
228 summarized in Table 1. A detailed description of the parameterization is provided in the Supplement
229 (Section S2). Considering that there remain significant uncertainties in the key parameters (i.e., the
230 uptake coefficient of NO_2 on aerosol or ground surfaces, EF, and HONO emission ratios) of the
231 heterogeneous HONO formation pathways and its direct emissions as listed in Table 1, we
232 performed the sensitivity analyses for these parameters to evaluate their influences on the model



233 results.

234

235 In addition, we included the dry deposition of HNO₃ with a velocity (v_{HNO_3}) of 0.0175 m s⁻¹ (Liu
236 et al., 2019). The rate constant of the deposition was then calculated using eq. 5:

$$237 \quad k_{\text{dep}} = \frac{v_{\text{HNO}_3}}{\text{PBL}} \quad (5)$$

238 where PBL is the planetary boundary layer height. We also considered the dilution of all other
239 species via deposition, entrainment, etc. using a highly simplified parameterization:

$$240 \quad \frac{d[X]}{dt} = -k_{\text{dil}} ([X] - [X]_{\text{bkg}}) \quad (6)$$

241 where k_{dil} is the first-order dilution rate constant; $[X]_{\text{bkg}}$ is a fixed background concentration of
242 pollutants. Here, a typical dilution lifetime of one day was assumed, i.e., $k_{\text{dil}} = 1/86400 \text{ s}^{-1}$. As the
243 species background concentration was unknown, $[X]_{\text{bkg}}$ was set to 0 for simplicity.

244

245 In the model, the j values of various gaseous species were calculated using the default MCMv3.3.1
246 parameterization with input of the solar zenith angle at the observations sites and scaled by the ratio
247 of measured to calculated $j\text{NO}_2$ values. The observed pollutant concentrations and meteorological
248 parameters were used as the model input, which were updated hourly (one model step) using the
249 observation data and held constant during each model step, except for the observed concentrations
250 of NO and NO₂ (the sum of NO and NO₂ concentrations was also constrained by the observation).

251

252 3. Results and Discussion

253 3.1 Overview of pollution characteristics during winter

254 Table 2 shows the overall pollution conditions of the two observation sites in winter 2018 and 2019.
255 The average PM_{2.5} concentration increased by 17-21% in 2019 compared to that in 2018.
256 Accordingly, nitrate concentration also increased by 11-14% in 2019. The O₃ concentration was
257 slightly higher in 2019 than in 2018, consistent with increased atmospheric oxidation capacity in
258 recent years (Lu et al., 2018; Li et al., 2019b; Liu and Wang, 2020; Yang et al., 2020). In the two
259 years, both of the PM_{2.5} and nitrate concentrations at the Qingpu site were higher than those at the
260 Pudong site. As mentioned above, the Qingpu site is at the junction of Shanghai, Jiangsu, and
261 Zhejiang, so it is more easily influenced by the transport of air pollutants from Jiangsu, which is
262 usually more polluted than Shanghai. Besides, the average temperature at the Qingpu site was also
263 slightly lower than that at the Pudong site, which might to some extent favor the gas-to-particle
264 partitioning of HNO₃. Notably, the average RH was as high as 80% during the observation period,
265 which was significantly higher than that (63%) recorded in 2016 (Tao et al., 2016). In particular, the
266 RH exceeded 90% for more than one third of the days during the observation period.

267

268 Taking the Pudong site in 2019 as an example, we analyzed the time series of PM_{2.5}, nitrate, and
269 other related parameters and presented the results in Figure 3 (Time series of the pollutants at the
270 Qingpu site can be seen in Section S3 and Figure S2). PM_{2.5} pollution events occurred frequently in



271 the eastern YRD during winter. During the observation period, the $PM_{2.5}$ concentration exceeded 75
272 $\mu\text{g m}^{-3}$ for 34 days and $150 \mu\text{g m}^{-3}$ for 6 days. During the pollution episodes ($PM_{2.5} > 75 \mu\text{g m}^{-3}$),
273 nitrate had become the most important component of $PM_{2.5}$, and its concentration was a factor of
274 2.2 higher than that of sulfate. In winter, the emission of NO_x was obviously high. During the periods
275 with high nitrate concentration, the NO_x concentration always exceeded 100 ppb. The O_3
276 concentration was also at a relatively high level, with a maximum value of 60 ppb and an average
277 of 22 ppb, which was much higher than the wintertime average O_3 concentration (6-16 ppb) in the
278 NCP (Li et al., 2019a; Duan et al., 2020; Liu et al., 2020). The concentration of odd oxygen
279 ($O_x = O_3 + NO_2$) ranged between 20-83 ppb with an average of 44 ppb, indicating a relatively high
280 atmospheric oxidation capacity in the eastern YRD during winter. Consistently, the nitrogen
281 oxidation ratio (NOR, $NOR = NO_3 / (NO_3 + NO_2)$) was up to 0.51, suggesting a high degree of
282 atmospheric oxidation. Meanwhile, the high atmospheric RH in the eastern YRD led to a high
283 ALWC. During the high nitrate periods, the ALWC was often at its peak and could exceed $200 \mu\text{g}$
284 m^{-3} on rainy or haze-foggy days. Such a high ALWC level would have an important impact on the
285 nitrate formation. Notably, the NO_x concentration dropped sharply on 23 January and kept at a low
286 level until the end of the observation (12 February, 2020). This is mainly a result of marked emission
287 reductions during the COVID-19 lockdown. Such an emission reduction had a complicated
288 influence on the nitrate formation chemistry, which will be discussed in detail in Section 3.5.

289

290 Figure 4 shows the mass ratio of nitrate to $PM_{2.5}$ as a function of the $PM_{2.5}$ concentration and ALWC
291 at Qingpu and Pudong sites in 2018 and 2019. The ratio of nitrate to $PM_{2.5}$ increased with increasing
292 $PM_{2.5}$ concentration. When the $PM_{2.5}$ concentration was above $75 \mu\text{g m}^{-3}$, the average mass fraction
293 of nitrate was more than 30%. In addition, the nitrate formation rate was much higher than that of
294 sulfate and ammonium during $PM_{2.5}$ pollution episodes, as indicated by the slope of nitrate vs. $PM_{2.5}$
295 that was twice that of the other two ions (see Figure S3). These results indicate that the formation
296 of nitrate played a driving role in the formation of $PM_{2.5}$ pollution. In general, when the ALWC was
297 high, the nitrate concentration was also at a high level. On one hand, ALWC could promote the
298 nitrate formation by favoring the heterogeneous hydrolysis of N_2O_5 and the gas-to-particle
299 partitioning of HNO_3 . On the other hand, the increase in nitrate concentration could enhance the
300 hygroscopicity of $PM_{2.5}$, leading to an increase in ALWC, which would further promote the nitrate
301 formation (Wang et al., 2020b). It is worth noting that, when $PM_{2.5} < 100 \mu\text{g m}^{-3}$, the mass ratio of
302 NO_3 to $PM_{2.5}$ increased rapidly with rising $PM_{2.5}$ concentration, but when the $PM_{2.5}$ concentration
303 exceeded $100 \mu\text{g m}^{-3}$, the ratio reached a plateau. This might be due to the fact that when the $PM_{2.5}$
304 concentration increased to a certain level, the formation process of other components may also speed
305 up, causing the nitrate proportion to stay basically constant.

306

307 3.2 Gas-to-particle partitioning of nitrate

308 The gas-to-particle partitioning of nitrate determines the sensitivity of particulate nitrate formation
309 to the production of HNO_3 . Figure 5 shows the particulate nitrate concentration (measured) and its
310 fraction to total nitrate (ε_{HNO_3} , $\varepsilon_{HNO_3} = NO_3 / (NO_3 + HNO_3)$), predicted by ISORROPIA-II) as a



311 function of ALWC and aerosol pH. In order to avoid the influence of rainy and foggy days during
312 the observation period which could lead to the abnormal high ALWC, we only used the data with
313 RH below 95% for analysis. Obviously, ALWC promoted the formation of particulate nitrate, but
314 such a promoting effect varied greatly under different aerosol pH (top panel in Figures 5a-d). As the
315 pH increased, the slope of nitrate vs. ALWC also increased significantly, indicating a stronger
316 promoting effect. ALWC plays a dual role in the formation of nitrate aerosol: it can promote the
317 heterogeneous formation of nitrate, e.g., via N_2O_5 hydrolysis, by providing more reaction medium
318 and decreasing the kinetic limitation (Mozurkewich and Calvert, 1988; Bertram and Thornton, 2009;
319 Wang et al., 2020b); the ALWC can also promote the gas-to-particle partitioning of HNO_3 . The
320 different promoting effect of ALWC under different aerosol pH is mainly due to the fact that pH can
321 significantly influence the gas-to-particle partitioning of HNO_3 . As shown in Figures 5a-d (bottom
322 panel), when the aerosol pH was low, the gas-to-particle partitioning of HNO_3 was inhibited, with
323 the value of ϵ_{HNO_3} basically below 0.6 at $pH < 2$. Under these conditions, the increase of particulate
324 nitrate concentration would require more ALWC. When the pH increased, the inhibition effect of
325 pH on the gas-to-particle partitioning of HNO_3 was weakened. When the pH was higher than 2.5,
326 the nitrate was almost in the particle phase ($\epsilon_{HNO_3}=1$). As a result, the increase of ALWC would
327 rapidly promote the nitrate formation, particularly when ALWC was at a low level. It is important
328 to point out that during the whole observation period, the values of ϵ_{HNO_3} were larger than 0.9 for
329 90% of time when the $PM_{2.5}$ concentration was higher than $75 \mu g m^{-3}$ (see Figure S4). This indicates
330 that the gas-to-particle partitioning of HNO_3 was very efficient and not a limiting factor for
331 particulate nitrate formation during the pollution episodes. The gas-to-particle partitioning of HNO_3
332 was also efficient in the NCP region, and its average ϵ_{HNO_3} could reach 100% during the haze
333 pollution period (Guo et al., 2018; Li et al., 2019a). However, the average ϵ_{HNO_3} in the northeastern
334 United States during winter was only 39% (Guo et al., 2018), this might be due to the relatively
335 lower pH in this region (0.8 ± 1.0) (Guo et al., 2016), which inhibited the gas-to-particle partitioning.
336

337 3.3 Observational constraints on the nitrate formation mechanism

338 The nitrate formation mechanism is different during the different time of a day. The heterogeneous
339 hydrolysis of N_2O_5 was often found to be an important pathway for nighttime nitrate formation.
340 Here, we evaluated the role of this pathway to nitrate formation in the eastern YRD using the
341 correlation between particulate nitrate concentration and the production of N_2O_5 during nighttime.
342 Due to the lack of direct observational data of N_2O_5 in this study, we used the value of square of
343 NO_2 multiplied by O_3 ($[NO_2]^2 \times O_3$) to indicate the N_2O_5 level (Liu et al., 2020). Figure 6 shows the
344 nitrate concentration as a function of $[NO_2]^2 \times O_3$ during the nighttime in winter. The particulate
345 nitrate concentration showed a strong positive correlation with $[NO_2]^2 \times O_3$. In particular in 2018, as
346 the value of $[NO_2]^2 \times O_3$ increased to 15000, the nitrate concentration increased from 5-10 $\mu g m^{-3}$ to
347 25-30 $\mu g m^{-3}$, suggesting that the heterogeneous hydrolysis of N_2O_5 was an important pathway for
348 wintertime nitrate formation in the eastern YRD. Notably, there are some data points with low values
349 of $[NO_2]^2 \times O_3$ but high nitrate concentrations. This might be partly due to their relatively high
350 aerosol pH (> 3), which could promote the gas-to-particle partitioning of HNO_3 .



351 To evaluate the role of the gas-phase OH + NO₂ process in nitrate formation during the daytime, we
352 use the O_x to indicate the atmospheric oxidation capacity due to the lack of direct observational data
353 of OH radicals. Figure 7 shows the particulate nitrate concentration as a function of O_x during the
354 daytime. Notably, as the O_x concentration increased, the nitrate concentration also increased
355 significantly. However, the increase in ALWC seemed to have a relatively small impact on the
356 nitrate concentration during the daytime, indicating that the reaction of NO₂ with OH radicals to
357 form HNO₃ (rather than the gas-to-particle partitioning) was a rate-limiting step in daytime nitrate
358 formation. We also note that there are some data points with low O_x values but high ALWC and
359 nitrate concentrations (Figure 7c). This phenomenon might be owing to a certain degree of
360 heterogeneous process in the haze-foggy days, when the photochemical reactions were relatively
361 weaker. Overall, the high atmospheric oxidation capacity made the gas-phase OH + NO₂ reaction
362 an important pathway for nitrate formation during the daytime in the eastern YRD.

363

364 3.4 Model constraints on the nitrate formation mechanism

365 To quantify the contribution of different formation mechanisms to wintertime nitrate formation in
366 the eastern YRD, we used an observation-constrained model (FOAM v3.1) updated with the
367 heterogeneous chemistry of N₂O₅ and NO₂ (see Section 2.3 for details) to simulate the formation
368 rate of HNO₃ from different pathways during the observation period. During the winter of 2019, six
369 haze pollution episodes (PM_{2.5} > 75 μg m⁻³) occurred at both sites (there was an additional episode
370 during the outbreak of COVID-19 epidemic, which was discussed separately in Section 3.5). We
371 conducted simulations for all the six pollution episodes and took two representative ones at the
372 Pudong site for the detailed analysis. Considering the large uncertainties in ALWC estimation and
373 aerosol surface area/volume correction at high RH levels (> 95%), which could significantly affect
374 the simulation results, we excluded the simulated data above 95% RH from the further analysis.
375 Figure 8 shows the time series of various particulate (measured) and gaseous (measured and
376 simulated) air pollutants, as well as the formation rate of HNO₃ (simulated) from different pathways
377 during these two episodes (The case studies of the same episodes at the Qingpu site are given in
378 Section S4 and Figure S5).

379

380 In episode 1 (Figure 8a), the nitrate concentration increased rapidly from 15.2 μg m⁻³ at 22:00 on
381 29 December to 39.0 μg m⁻³ at 10:00 on 30 December, with an average growth rate of 2.0 μg m⁻³ h⁻¹.
382 The simulated NO₂ concentration was in good agreement with the observation, except for a short
383 period around the midnight of 30 December, during which the NO emissions led to an over-
384 prediction of the NO₂ level. During the high nitrate periods, the nighttime N₂O₅ concentration could
385 reach 0.5-1 ppb and contributed noticeably to HNO₃ formation via the heterogeneous hydrolysis.
386 However, the high daytime OH concentration (up to 2.5 × 10⁶ molecules cm⁻³) facilitated a relatively
387 more rapid nitrate formation from the gas-phase OH + NO₂ pathway. The average production rate
388 of HNO₃ from the gas-phase OH + NO₂ reaction during the daytime was 2.9 μg m⁻³ h⁻¹, which was
389 twice the average production rate of HNO₃ from the heterogeneous hydrolysis of N₂O₅ during the
390 nighttime.



391

392 We note that the overestimation of NO_2 during the night of 30 December (case 1) could lead to an
393 overestimation of nighttime HONO, but it did not significantly affect the overall production rate of
394 HONO and thereby OH radicals in this case, which was dominated by the daytime heterogeneous
395 photochemical processes (see Figure S7, HONO production rate in the base scenario). In addition,
396 as the O_3 concentration in the model was constrained by the measured value, which was very low
397 (< 5 ppb) during this time, the overestimation of NO_2 would also not significantly affect the
398 prediction of N_2O_5 . As a result, the over-prediction of NO_2 would not have a large influence on the
399 major formation pathways of nitrate.

400

401 There were two cases in the episode 2 (Figure 8b). In case 2, the concentration of nitrate increased
402 from $26.8 \mu\text{g m}^{-3}$ at 05:00 to $46.0 \mu\text{g m}^{-3}$ at 13:00 on 12 January, 2020, with an average growth rate
403 of $2.4 \mu\text{g m}^{-3} \text{h}^{-1}$. Then, the nitrate concentration achieved a fast growth from 40.2 to $70.5 \mu\text{g m}^{-3}$
404 within only six hours during the night of 12 January, with an average rate of $5.1 \mu\text{g m}^{-3} \text{h}^{-1}$. During
405 the nitrate increasing period, the maximum OH concentration was $\sim 1.0 \times 10^6$ molecules cm^{-3} . As a
406 result, the gas-phase OH+ NO_2 reaction led to a slow increase of nitrate concentration in the daytime
407 of 12 January. During the nighttime, the N_2O_5 concentration quickly increased to 0.83 ppb. The high
408 N_2O_5 level, in combination with the high ALWC, made the heterogeneous hydrolysis of N_2O_5 a
409 more important pathway for nitrate formation. The simulated average production rate of HNO_3 from
410 the heterogeneous hydrolysis of N_2O_5 during this case was $4.0 \mu\text{g m}^{-3} \text{h}^{-1}$, which was 3.6 times that
411 of the formation rate from the gas-phase OH + NO_2 reaction ($1.1 \mu\text{g m}^{-3} \text{h}^{-1}$). In case 3, the nitrate
412 concentration increased from $22.5 \mu\text{g m}^{-3}$ at 0:00 to $53.8 \mu\text{g m}^{-3}$ at 11:00 on 14 January, with an
413 average growth rate of $2.8 \mu\text{g m}^{-3} \text{h}^{-1}$. The N_2O_5 concentration was at a high level (~ 1 ppb) during
414 the nighttime and its hydrolysis contributed significantly to nitrate formation at the beginning of the
415 nitrate-increasing period. In the morning of 14 January, the OH concentration rapidly increased to
416 1.3×10^6 molecules cm^{-3} , resulting in considerable nitrate formation from the gas-phase process.
417 The average production rates of HNO_3 from the heterogeneous and gas-phase processes in this case
418 were 3.9 and $2.4 \mu\text{g m}^{-3} \text{h}^{-1}$, respectively, suggesting that both processes were important nitrate
419 formation pathways.

420

421 As mentioned above, there were six haze pollution episodes during the observation period. At the
422 Qingpu site, the heterogeneous hydrolysis of N_2O_5 was the major formation pathway (65-80%) of
423 nitrate aerosol for four episodes, while the gas-phase OH + NO_2 reaction had a major contribution
424 (54-60%) for the other two episodes. At the Pudong site, the heterogeneous process also contributed
425 dominantly (67-89%) to nitrate formation during four episodes, and for the other two episodes, the
426 contributions of the heterogeneous and gas-phase processes were comparable (51-53% vs. 45-47%).
427 Figure S6 shows the average diurnal variation of the production rates of HNO_3 from different
428 pathways during the observation period in 2019. The gas-phase process produced HNO_3 mainly
429 from 7:00 to 16:00, while the HNO_3 production from the heterogeneous process occurred mainly
430 from 17:00 to 6:00. The average production rates of HNO_3 from the heterogeneous and gas-phase



431 processes are given in Figure 9. At the Qingpu site, the average production rate of HNO₃ from the
432 two processes was 3.79 μg m⁻³ h⁻¹ for the heterogeneous process during the nighttime (14 hours) vs.
433 2.94 μg m⁻³ h⁻¹ for the gas-phase reaction during the daytime (10 hours). The production rate from
434 other processes such as NO₂ hydrolysis and NO₃ radical oxidation of VOCs was only 0.08 μg m⁻³
435 h⁻¹. Therefore, the heterogeneous and gas-phase processes contributed to 63% and 35% of nitrate
436 formation at this site, respectively. At the Pudong site, the average formation rate of HNO₃ from the
437 hydrolysis of N₂O₅ was 3.83 μg m⁻³ h⁻¹, significantly higher than that from the gas-phase reaction
438 (2.27 μg m⁻³ h⁻¹). As a result, the contributions of heterogeneous and gas-phase processes to nitrate
439 formation were 69% and 29%, respectively.

440

441 It should be noted that significant uncertainties remain in the key parameters of the heterogeneous
442 HONO formation pathways in the model, which could affect the prediction of the OH level and
443 thereby gas-phase formation of HNO₃. However, sensitive analyses for various parameters show
444 that the current parameterization of these heterogeneous reactions in the model (see Table 1) allows
445 for robust quantitative constraints on the relative contributions of the gas-phase and heterogeneous
446 processes to nitrate formation during haze pollution episodes (see Section S5 and Figure S7 for more
447 details).

448

449 As discussed in Section 3.2, the gas-to-particle partitioning of HNO₃ was rather efficient, with the
450 value of ε_{HNO₃} larger than 0.9 for 90% of the time during the haze pollution periods. Therefore,
451 the overall formation rate of particulate nitrate would be determined by the production rate of HNO₃
452 from the heterogeneous hydrolysis of N₂O₅ and gas-phase OH + NO₂ reaction. To identify the key
453 chemical factors that controlled the production rates of HNO₃ from these two major reaction
454 pathways, the relationships between the HNO₃ production rate and concentrations of NO₂ and
455 oxidants (i.e., O₃ or OH radicals) are examined and plotted in Figure 10.

456

457 As shown in Figure 10a, the slopes of the HNO₃ production rate from the heterogeneous process vs.
458 NO₂ during the nighttime were different under different O₃ concentrations. When O₃ concentrations
459 were higher than 10 ppb, the increase in NO₂ led to a significant increase in HNO₃ production, with
460 the production rate exceeding 5 μg m⁻³ h⁻¹ when the NO₂ was higher than 30 ppb. However, when
461 the O₃ level was low (< 10 ppb), the heterogeneous process was relatively slow, even with NO₂
462 concentration exceeding 60 ppb. These results suggest that the atmospheric oxidation capacity (or
463 the availability of O₃), which affected the production of N₂O₅, played a vital role in controlling the
464 nitrate formation rate from the heterogeneous process. Furthermore, the reactive uptake of N₂O₅ by
465 aerosols was found to be very efficient (see Figure S8) so that it was not the rate-limiting step of the
466 heterogeneous nitrate formation during the haze pollution periods. Similarly, the slope of the HNO₃
467 production rate from the gas-phase process vs. NO₂ during the daytime also varied dramatically
468 under different OH radical concentrations (Figure 10b). As the OH radical concentration was higher
469 than 7 × 10⁵ molecules cm⁻³, this rate increased markedly with the increase in NO₂. This
470 phenomenon proved again that the atmospheric oxidation capacity played a driving role in the



471 production of HNO_3 from the gas-phase process.

472

473 The results in Figure 10 also suggest that solely reducing the NO_x emissions might result in an
474 increase of O_3 and OH concentrations, which could enhance the oxidation of NO_x and thereby offset
475 the effect of NO_x emission reductions on HNO_3 production. Therefore, a synergistic control of
476 atmospheric oxidant and NO_x emissions would be of great importance for mitigating wintertime
477 particulate nitrate pollution in the eastern YRD.

478

479 **3.5 Nitrate aerosol formation during the COVID-19**

480 The city lockdowns during the COVID-19 epidemic resulted in substantial emission reductions from
481 vehicular and industrial sources, which provided an opportunity to investigate the response of
482 secondary aerosols to primary emission reductions. Here, we selected the 23 January, 2019 as a
483 demarcation point (since then many cities in China started to implement lockdown measures) and
484 analyzed the characteristics of particulate nitrate pollution before and during the COVID-19
485 epidemic.

486

487 Figure 11 shows the concentrations of major gaseous and particulate air pollutants, NOR, and sulfur
488 oxidation ratio (SOR) in the eastern YRD before (1-22 January, 2020) and during (23 January-12
489 February, 2020) the COVID-19 epidemic. At the Pudong site (Figure 11 a, b, c), the average NO_x
490 concentration decreased by 57% due to marked reductions in vehicular emissions during the
491 epidemic. In contrast, the SO_2 concentration only had a small decrease (16%) during the epidemic,
492 since it mainly comes from coal-combustion sources and is less affected by vehicular emissions.
493 However, the O_3 concentration increased by 66% during the epidemic. This is mainly due to the
494 significant reduction in NO_x emissions, though the changes in meteorological conditions could also
495 contribute (Zhao et al., 2020b). Accordingly, the model simulations show that the atmospheric OH
496 concentration (median) increased by 14% during the epidemic, though the average value only
497 increased slightly. The increase in O_3 and OH concentrations could significantly promote the
498 oxidation of NO_x to nitrate and SO_2 to sulfate through both gas-phase and heterogeneous processes.
499 As shown in Figure 11c, the average values of NOR and SOR increased from 0.15 and 0.46 before
500 the epidemic to 0.21 and 0.50 during the epidemic, respectively. The enhanced oxidation of NO_x
501 and SO_2 would weaken the response of particulate nitrate and sulfate to the emission reductions. As
502 can be seen in Figure 11b and c, the simulated HNO_3 production rate and measured particulate nitrate
503 concentration dropped by 42% and 40% during the epidemic, respectively, which were both
504 significantly smaller than the decrease in NO_x concentration (57%), while the particulate sulfate
505 concentration only decreased by 2%, also substantially smaller than the reduction in SO_2
506 concentration (16%).

507

508 Similarly, at the Qingpu site, the NO_x concentration decreased by 58% during the epidemic, while
509 the concentrations of O_3 and OH radicals (median) increased by 90% and 17%, respectively. The
510 significantly enhanced atmospheric oxidation capacity made the simulated HNO_3 production rate



511 only decrease by 17% during the epidemic. However, the measured particulate nitrate concentration
512 at this site decreased by 60%, comparable to the decrease in NO_x concentration. The inconsistency
513 between the decrease in measured nitrate concentration and simulated HNO_3 production rate at the
514 Qingpu site was different from the situation observed at the Pudong site, which is likely due to the
515 fact that the Qingpu site was more easily to be influenced by the regional transport. We note that the
516 average wind speed at the Qingpu site (1.8 m s^{-1}) was higher than that at the Pudong site (1.1 m s^{-1}).
517 Besides, the haze pollution was more serious at the Qingpu site than at the Pudong site before
518 the epidemic: both $\text{PM}_{2.5}$ and nitrate concentrations were significantly higher at the Qingpu site (see
519 Figure 11). Therefore, the marked emission reductions on a regional scale during the epidemic
520 would decrease both the local formation and transport of particulate nitrate from the upwind regions,
521 resulting in a more pronounced reduction in observed nitrate concentration at the Qingpu site. In
522 addition, as air plume influenced by the regional transport was more aged, the NOR and SOR values
523 before the epidemic were even higher than those during the epidemic.

524

525 The results at the Pudong site clearly show that the enhanced atmospheric oxidation capacity during
526 the COVID-19 epidemic promoted the formation of secondary aerosols and offset the effects of
527 primary emission reductions in the eastern YRD. Such a phenomenon has also been observed in
528 many other regions in China during the COVID-19 lockdown (Le et al., 2020; Zheng et al., 2020;
529 Huang et al., 2021; Liu et al., 2021; Tian et al., 2021; Zhong et al., 2021). These results suggest an
530 important role of atmospheric oxidation capacity in regulating secondary aerosol formation. They
531 also highlight the importance of the synergetic regulation of atmospheric oxidants and other air
532 pollutants in the mitigation of particulate pollution in China. However, the Qingpu site also provided
533 us a special case that in severely polluted regions with a stronger influence from the regional
534 transport, the offset effects of enhanced atmospheric oxidation capacity on emission reductions
535 could be more complicated and less significant.

536

537 4. Conclusions

538 In this study, the chemical mechanisms and key controlling factors of wintertime nitrate formation
539 in the eastern YRD of China were investigated using a combination of online field observations and
540 detailed model simulations. During the observation period (Winter 2018 and 2019), the haze
541 pollution events ($\text{PM}_{2.5} > 75 \mu\text{g m}^{-3}$) occurred frequently in this region. The mass fraction of nitrate
542 in $\text{PM}_{2.5}$ increased dramatically with $\text{PM}_{2.5}$ concentration and exceeded 30% throughout the
543 pollution periods. The measured nitrate concentration was well correlated with $[\text{NO}_2]^2 \times [\text{O}_3]$ (an
544 indicator of N_2O_5) at night and the level of O_x (an indicator of atmospheric oxidation capacity)
545 during the daytime, indicating that both the heterogeneous hydrolysis of N_2O_5 and gas-phase $\text{OH} +$
546 NO_2 process played important roles in wintertime nitrate formation in the eastern YRD.
547 Observation-constrained model simulations further show that the average production rates of HNO_3
548 from the heterogeneous hydrolysis of N_2O_5 during the nighttime and gas-phase $\text{OH} + \text{NO}_2$ reaction
549 during the daytime were $3.81 \mu\text{g m}^{-3} \text{ h}^{-1}$ and $2.61 \mu\text{g m}^{-3} \text{ h}^{-1}$, respectively, during the haze pollution
550 periods; these two pathways accounted for 66% and 32% of wintertime nitrate formation in the



551 eastern YRD, respectively.

552

553 The ALWC significantly promoted the formation of nitrate by facilitating the hydrolysis of N_2O_5
554 and the gas-to-particle partitioning of HNO_3 . However, the promoting effect of ALWC on nitrate
555 formation varied with aerosol pH due to its significant influence on the gas-to-particle partitioning
556 of HNO_3 . During the pollution periods, the gas-to-particle partitioning of HNO_3 was very efficient,
557 with the partitioning coefficients, ϵ_{HNO_3} , larger than 0.9 for 90% of the time. Therefore, the overall
558 formation processes of wintertime particulate nitrate were not limited by the gas-to-particle
559 partitioning of HNO_3 but rather by its production from both heterogeneous and gas-phase processes.
560 Further analyses of the response of HNO_3 formation to the variation in the concentrations of NO_2 ,
561 O_3 , and OH radicals suggests that the atmospheric oxidation capacity (i.e., the availability of O_3 and
562 OH radicals) played a key role in controlling the formation of nitrate from both processes.

563

564 During the COVID-19 lockdown (January-February 2020), the enhanced atmospheric oxidation
565 capacity promoted the oxidation of NO_x to nitrate and weaken the effects of primary emission
566 reductions on particulate pollution in typical urban areas in the eastern YRD, though such an offset
567 effect was less significant in regions with a stronger influence from the regional transport. This
568 phenomenon again suggests that the atmospheric oxidation capacity played an important role in
569 driving the formation of secondary aerosols, and highlights the importance of the synergetic
570 regulation of atmospheric oxidation capacity and other air pollutants in the mitigation of particulate
571 pollution in eastern China.

572

573 *Data availability.* The data presented in this work are available upon request from the corresponding
574 authors.

575

576 *Author contributions.* YZ designed the study, JH, QZ, QF, and YD performed field measurements,
577 JYS conducted ISORROPIA-II model calculation, JA and CH provided the NO_x emission inventory,
578 and YZ and HZ analyzed the data, conducted model simulations, and wrote the paper. All other
579 authors contributed to discussion and writing.

580

581 *Competing interests.* The authors declare no conflict of interest.

582

583 *Acknowledgments.* This work was supported by the National Natural Science Foundation
584 of China (Grant # 22022607) and the Science and Technology Commission of Shanghai
585 Municipality (Grant # 19DZ1205004). Yue Zhao acknowledges the Program for Professor
586 of Special Appointment (Eastern Scholar) at Shanghai Institutions of Higher Learning.

587

588 **References:**

589 Alexander, B., Sherwen, T., Holmes, C. D., Fisher, J. A., Chen, Q., Evans, M. J., and Kasibhatla, P.:
590 Global inorganic nitrate production mechanisms: comparison of a global model with nitrate isotope
591 observations, *Atmos. Chem. Phys.*, 20, 3859–3877, 10.5194/acp-20-3859-2020, 2020.



- 592 Bertram, T. H. and Thornton, J. A.: Toward a general parameterization of N₂O₅ reactivity on aqueous
593 particles: the competing effects of particle liquid water, nitrate and chloride, *Atmos. Chem. Phys.*, 9,
594 8351-8363, 2009.
- 595 Bertram, T. H., Thornton, J. A., Riedel, T. P., Middlebrook, A. M., Bahreini, R., Bates, T. S., Quinn, P.
596 K., and Coffman, D. J.: Direct observations of N₂O₅ reactivity on ambient aerosol particles, *Geophys.
597 Res. Lett.*, 36, 2009.
- 598 Brown, S. S. and Stutz, J.: Nighttime radical observations and chemistry, *Chem. Soc. Rev.*, 41, 6405-
599 6447, 2012.
- 600 Calvert, J. G. and Stockwell, W. R.: Acid generation in the troposphere by gas-phase chemistry, *Environ.
601 Sci. Technol.*, 17, 428A-443A, 1983.
- 602 Chan, Y. C., Evans, M. J., He, P., Holmes, C. D., Jaeglé, L., Kasibhatla, P., Liu, X. Y., Sherwen, T.,
603 Thornton, J. A., Wang, X., Xie, Z., Zhai, S., and Alexander, B.: Heterogeneous Nitrate Production
604 Mechanisms in Intense Haze Events in the North China Plain, *J. Geophys. Res.-Atmos.*, 126,
605 10.1029/2021jd034688, 2021.
- 606 Chen, X., Wang, H., Liu, Y., Su, R., Wang, H., Lou, S., and Lu, K.: Spatial characteristics of the nighttime
607 oxidation capacity in the Yangtze River Delta, China, *Atmos. Environ.*, 208, 150-157,
608 10.1016/j.atmosenv.2019.04.012, 2019.
- 609 Chen, X., Wang, H., Lu, K., Li, C., Zhai, T., Tan, Z., Ma, X., Yang, X., Liu, Y., Chen, S., Dong, H., Li,
610 X., Wu, Z., Hu, M., Zeng, L., and Zhang, Y.: Field Determination of Nitrate Formation Pathway in
611 Winter Beijing, *Environ. Sci. Technol.*, 54, 9243-9253, 10.1021/acs.est.0c00972, 2020.
- 612 Ding, A., Fu, C., Yang, X., Sun, J., Zheng, L., Xie, Y., Herrmann, E., Nie, W., Petäjä, T., and Kerminen,
613 V.-M.: Ozone and fine particle in the western Yangtze River Delta: an overview of 1 yr data at the
614 SORPES station, *Atmos. Chem. Phys.*, 13, 5813-5830, 2013.
- 615 Ding, A., Huang, X., Nie, W., Chi, X., Xu, Z., Zheng, L., Xu, Z., Xie, Y., Qi, X., Shen, Y., Sun, P., Wang,
616 J., Wang, L., Sun, J., Yang, X.-Q., Qin, W., Zhang, X., Cheng, W., Liu, W., Pan, L., and Fu, C.:
617 Significant reduction of PM_{2.5} in eastern China due to regional-scale emission control: evidence from
618 SORPES in 2011–2018, *Atmos. Chem. Phys.*, 19, 11791-11801, 10.5194/acp-19-11791-2019, 2019.
- 619 Duan, J., Huang, R.-J., Li, Y., Chen, Q., Zheng, Y., Chen, Y., Lin, C., Ni, H., Wang, M., Ovadnevaite, J.,
620 Ceburnis, D., Chen, C., Worsnop, D. R., Hoffmann, T., O'Dowd, C., and Cao, J.: Summertime and
621 wintertime atmospheric processes of secondary aerosol in Beijing, *Atmos. Chem. Phys.*, 20, 3793-
622 3807, 10.5194/acp-20-3793-2020, 2020.
- 623 Fang, Y., Ye, C., Wang, J., Wu, Y., Hu, M., Lin, W., Xu, F., and Zhu, T.: Relative humidity and O₃
624 concentration as two prerequisites for sulfate formation, *Atmos. Chem. Phys.*, 19, 12295-12307,
625 10.5194/acp-19-12295-2019, 2019.
- 626 Fountoukis, C. and Nenes, A.: ISORROPIA II: a computationally efficient thermodynamic equilibrium
627 model for K⁺-Ca²⁺-Mg²⁺-NH₄⁺-Na⁺-SO₄²⁻-NO₃⁻-Cl⁻-H₂O aerosols, *Atmos. Chem. Phys.*, 7, 4639-
628 4659, 2007.
- 629 Fu, X., Wang, T., Gao, J., Wang, P., Liu, Y., Wang, S., Zhao, B., and Xue, L.: Persistent Heavy Winter
630 Nitrate Pollution Driven by Increased Photochemical Oxidants in Northern China, *Environ. Sci.
631 Technol.*, 54, 3881-3889, 10.1021/acs.est.9b07248, 2020.
- 632 Guo, H., Otjes, R., Schlag, P., Kiendler-Scharr, A., Nenes, A., and Weber, R. J.: Effectiveness of ammonia
633 reduction on control of fine particle nitrate, *Atmos. Chem. Phys.*, 18, 12241-12256, 2018.
- 634 Guo, H., Sullivan, A. P., Campuzano-Jost, P., Schroder, J. C., Lopez-Hilfiker, F. D., Dibb, J. E., Jimenez,
635 J. L., Thornton, J. A., Brown, S. S., and Nenes, A.: Fine particle pH and the partitioning of nitric acid
636 during winter in the northeastern United States, *J. Geophys. Res.-Atmos.*, 121, 10,355-310,376, 2016.
- 637 Guo, H., Xu, L., Bougiatioti, A., Cerully, K. M., Capps, S. L., Hite Jr, J., Carlton, A., Lee, S.-H., Bergin,
638 M., and Ng, N.: Fine-particle water and pH in the southeastern United States, *Atmos. Chem. Phys.*,
639 15, 5211-5228, 2015.
- 640 Han, C., Yang, W., Wu, Q., Yang, H., and Xue, X.: Heterogeneous photochemical conversion of NO₂ to
641 HONO on the humic acid surface under simulated sunlight, *Environ. Sci. Technol.*, 50, 5017-5023,
642 2016.
- 643 He, P., Xie, Z., Chi, X., Yu, X., Fan, S., Kang, H., Liu, C., and Zhan, H.: Atmospheric Δ¹⁷O(NO₃) reveals
644 nocturnal chemistry dominates nitrate production in Beijing haze, *Atmos. Chem. Phys.*, 18, 14465-
645 14476, 10.5194/acp-18-14465-2018, 2018.
- 646 Hennigan, C., Izumi, J., Sullivan, A., Weber, R., and Nenes, A.: A critical evaluation of proxy methods
647 used to estimate the acidity of atmospheric particles, *Atmos. Chem. Phys.*, 15, 2775-2790, 2015.
- 648 Hua, Y., Cheng, Z., Wang, S., Jiang, J., Chen, D., Cai, S., Fu, X., Fu, Q., Chen, C., and Xu, B.:
649 Characteristics and source apportionment of PM_{2.5} during a fall heavy haze episode in the Yangtze



- 650 River Delta of China, *Atmos. Environ.*, 123, 380-391, 2015.
- 651 Huang, R.-J., He, Y., Duan, J., Li, Y., Chen, Q., Zheng, Y., Chen, Y., Hu, W., Lin, C., and Ni, H.:
652 Contrasting sources and processes of particulate species in haze days with low and high relative
653 humidity in wintertime Beijing, *Atmos. Chem. Phys.*, 20, 9101-9114, 2020.
- 654 Huang, R. J., Zhang, Y. L., Bozzetti, C., Ho, K. F., Cao, J. J., Han, Y. M., Daellenbach, K. R., Slowik, J.
655 G., Platt, S. M., Canonaco, F., Zotter, P., Wolf, R., Pieber, S. M., Bruns, E. A., Crippa, M., Ciarelli,
656 G., Piazzalunga, A., Schwikowski, M., Abbazade, G., Schnelle-Kreis, J., Zimmermann, R., An, Z.
657 S., Szidat, S., Baltensperger, U., El Haddad, I., and Prevot, A. S. H.: High secondary aerosol
658 contribution to particulate pollution during haze events in China, *Nature*, 514, 218-222, 2014.
- 659 Huang, X., Ding, A., Gao, J., Zheng, B., Zhou, D., Qi, X., Tang, R., Wang, J., Ren, C., and Nie, W.:
660 Enhanced secondary pollution offset reduction of primary emissions during COVID-19 lockdown in
661 China, *Natl. Sci. Rev.* 8, nwa137, 2021.
- 662 Jenkin, M., Young, J., and Rickard, A.: The MCM v3.3.1 degradation scheme for isoprene, *Atmos. Chem.*
663 *Phys.*, 15, 11433-11459, 2015.
- 664 Kleffmann, J., Becker, K., and Wiesen, P.: Heterogeneous NO₂ conversion processes on acid surfaces:
665 possible atmospheric implications, *Atmos. Environ.*, 32, 2721-2729, 1998.
- 666 Kong, L., Yang, Y., Zhang, S., Zhao, X., Du, H., Fu, H., Zhang, S., Cheng, T., Yang, X., and Chen, J.:
667 Observations of linear dependence between sulfate and nitrate in atmospheric particles, *J. Geophys.*
668 *Res.-Atmos.*, 119, 341-361, 2014.
- 669 Kong, L., Feng, M., Liu, Y., Zhang, Y., Zhang, C., Li, C., Qu, Y., An, J., Liu, X., Tan, Q., Cheng, N.,
670 Deng, Y., Zhai, R., and Wang, Z.: Elucidating the pollution characteristics of nitrate, sulfate and
671 ammonium in PM_{2.5} in Chengdu, southwest China, based on 3-year measurements, *Atmos. Chem.*
672 *Phys.*, 20, 11181-11199, 10.5194/acp-20-11181-2020, 2020.
- 673 Kurtenbach, R., Becker, K., Gomes, J., Kleffmann, J., Lörzer, J., Spittler, M., Wiesen, P., Ackermann, R.,
674 Geyer, A., and Platt, U.: Investigations of emissions and heterogeneous formation of HONO in a road
675 traffic tunnel, *Atmos. Environ.*, 35, 3385-3394, 2001.
- 676 Le, T., Wang, Y., Liu, L., Yang, J., Yung, Y. L., Li, G., and Seinfeld, J. H.: Unexpected air pollution with
677 marked emission reductions during the COVID-19 outbreak in China, *Science*, 369, 702-706, 2020.
- 678 Lee, Y. and Schwartz, S. E.: Kinetics of oxidation of aqueous sulfur (IV) by nitrogen dioxide,
679 *Precipitation Scavenging, Dry Deposition and Resuspension*, 1, 453-470, 1983.
- 680 Lelieveld, J., Evans, J. S., Fnais, M., Giannadaki, D., and Pozzer, A.: The contribution of outdoor air
681 pollution sources to premature mortality on a global scale, *Nature*, 525, 367+, 2015.
- 682 Li, H., Cheng, J., Zhang, Q., Zheng, B., Zhang, Y., Zheng, G., and He, K.: Rapid transition in winter
683 aerosol composition in Beijing from 2014 to 2017: response to clean air actions, *Atmos. Chem. Phys.*,
684 19, 11485-11499, 2019a.
- 685 Li, H., Zhang, Q., Zheng, B., Chen, C., Wu, N., Guo, H., Zhang, Y., Zheng, Y., Li, X., and He, K.: Nitrate-
686 driven urban haze pollution during summertime over the North China Plain, *Atmos. Chem. Phys.*, 18,
687 5293-5306, 10.5194/acp-18-5293-2018, 2018.
- 688 Li, K., Jacob, D. J., Liao, H., Zhu, J., Shah, V., Shen, L., Bates, K. H., Zhang, Q., and Zhai, S.: A two-
689 pollutant strategy for improving ozone and particulate air quality in China, *Nat. Geosci.*, 12, 906-910,
690 2019b.
- 691 Li, M., Wang, T., Xie, M., Li, S., Zhuang, B., Huang, X., Chen, P., Zhao, M., and Liu, J.: Formation and
692 evolution mechanisms for two extreme haze episodes in the Yangtze River Delta region of China
693 during winter 2016, *J. Geophys. Res.-Atmos.*, 124, 3607-3623, 2019c.
- 694 Lin, Y.-C., Zhang, Y.-L., Fan, M.-Y., and Bao, M.: Heterogeneous formation of particulate nitrate under
695 ammonium-rich regimes during the high-PM_{2.5} events in Nanjing, China, *Atmos. Chem. Phys.*, 20,
696 3999-4011, 10.5194/acp-20-3999-2020, 2020.
- 697 Liu, L., Zhang, J., Du, R., Teng, X., Hu, R., Yuan, Q., Tang, S., Ren, C., Huang, X., and Xu, L.: Chemistry
698 of atmospheric fine particles during the COVID-19 pandemic in a megacity of Eastern China,
699 *Geophys. Res. Lett.*, 48, 2020GL091611, 2021.
- 700 Liu, P., Ye, C., Xue, C., Zhang, C., Mu, Y., and Sun, X.: Formation mechanisms of atmospheric nitrate
701 and sulfate during the winter haze pollution periods in Beijing: gas-phase, heterogeneous and
702 aqueous-phase chemistry, *Atmos. Chem. Phys.*, 20, 4153-4165, 10.5194/acp-20-4153-2020, 2020.
- 703 Liu, Y. and Wang, T.: Worsening urban ozone pollution in China from 2013 to 2017–Part 1: The complex
704 and varying roles of meteorology, *Atmos. Chem. Phys.*, 20, 6305-6321, 2020.
- 705 Liu, Y., Lu, K., Ma, Y., Yang, X., Zhang, W., Wu, Y., Peng, J., Shuai, S., Hu, M., and Zhang, Y.: Direct
706 emission of nitrous acid (HONO) from gasoline cars in China determined by vehicle chassis



- 707 dynamometer experiments, *Atmos. Environ.*, 169, 89-96, 2017.
- 708 Liu, Y., Lu, K., Li, X., Dong, H., Tan, Z., Wang, H., Zou, Q., Wu, Y., Zeng, L., Hu, M., Min, K. E.,
709 Kecorius, S., Wiedensohler, A., and Zhang, Y.: A Comprehensive Model Test of the HONO Sources
710 Constrained to Field Measurements at Rural North China Plain, *Environ. Sci. Technol.*, 53, 3517-
711 3525, 10.1021/acs.est.8b06367, 2019.
- 712 Lu, X., Hong, J., Zhang, L., Cooper, O. R., Schultz, M. G., Xu, X., Wang, T., Gao, M., Zhao, Y., and
713 Zhang, Y.: Severe surface ozone pollution in China: a global perspective, *Environ. Sci. Technol. Lett.*,
714 5, 487-494, 2018.
- 715 McDuffie, E. E., Womack, C. C., Fibiger, D. L., Dube, W. P., Franchin, A., Middlebrook, A. M.,
716 Goldberger, L., Lee, B., Thornton, J. A., Moravek, A., Murphy, J. G., Baasandorj, M., and Brown, S.
717 S.: On the contribution of nocturnal heterogeneous reactive nitrogen chemistry to particulate matter
718 formation during wintertime pollution events in Northern Utah, *Atmos. Chem. Phys.*, 19, 9287-9308,
719 10.5194/acp-19-9287-2019, 2019.
- 720 Mozurkewich, M. and Calvert, J. G.: Reaction probability of N_2O_5 on aqueous aerosols, *Journal of*
721 *Geophysical Research: Atmospheres*, 93, 15889-15896, 1988.
- 722 Peng, J. F., Hu, M., Shang, D. J., Wu, Z. J., Du, Z. F., Tan, T. Y., Wang, Y. N., Zhang, F., and Zhang, R.
723 Y.: Explosive Secondary Aerosol Formation during Severe Haze in the North China Plain, *Environ.*
724 *Sci. Technol.*, 55, 2189-2207, 10.1021/acs.est.0c07204, 2021.
- 725 Romer, P. S., Wooldridge, P. J., Crounse, J. D., Kim, M. J., Wennberg, P. O., Dibb, J. E., Scheuer, E.,
726 Blake, D. R., Meinardi, S., and Brosius, A. L.: Constraints on Aerosol Nitrate Photolysis as a
727 Potential Source of HONO and NO_x , *Environ. Sci. Technol.*, 52, 13738-13746, 2018.
- 728 Shao, P. Y., Tian, H. Z., Sun, Y. J., Liu, H. J., Wu, B. B., Liu, S. H., Liu, X. Y., Wu, Y. M., Liang, W. Z.,
729 Wang, Y., Gao, J. J., Xue, Y. F., Bai, X. X., Liu, W., Lin, S. M., and Hu, G. Z.: Characterizing
730 remarkable changes of severe haze events and chemical compositions in multi-size airborne particles
731 (PM_1 , $PM_{2.5}$ and PM_{10}) from January 2013 to 2016-2017 winter in Beijing, China, *Atmos. Environ.*,
732 189, 133-144, 10.1016/j.atmosenv.2018.06.038, 2018.
- 733 Shen, J., Zhao, Q., Cheng, Z., Wang, P., Ying, Q., Liu, J., Duan, Y., and Fu, Q.: Insights into source
734 origins and formation mechanisms of nitrate during winter haze episodes in the Yangtze River Delta,
735 *Sci. Total. Environ.*, 741, 140187, 10.1016/j.scitotenv.2020.140187, 2020.
- 736 Slater, E. J., Whalley, L. K., Woodward-Massey, R., Ye, C., Lee, J. D., Squires, F., Hopkins, J. R.,
737 Dunmore, R. E., Shaw, M., and Hamilton, J. F.: Elevated levels of OH observed in haze events during
738 wintertime in central Beijing, *Atmos. Chem. Phys.*, 20, 14847-14871, 2020.
- 739 Su, X., Tie, X., Li, G., Cao, J., Huang, R., Feng, T., Long, X., and Xu, R.: Effect of hydrolysis of N_2O_5
740 on nitrate and ammonium formation in Beijing China: WRF-Chem model simulation, *Science of the*
741 *Total Environment*, 579, 221-229, 2017.
- 742 Sun, P., Nie, W., Chi, X., Xie, Y., Huang, X., Xu, Z., Qi, X., Xu, Z., Wang, L., Wang, T., Zhang, Q., and
743 Ding, A.: Two years of online measurement of fine particulate nitrate in the western Yangtze River
744 Delta: influences of thermodynamics and N_2O_5 hydrolysis, *Atmos. Chem. Phys.*, 18, 17177-17190,
745 10.5194/acp-18-17177-2018, 2018.
- 746 Tan, Z., Fuchs, H., Lu, K., Hofzumahaus, A., Bohn, B., Broch, S., Dong, H., Gomm, S., Häseler, R., and
747 He, L.: Radical chemistry at a rural site (Wangdu) in the North China Plain: observation and model
748 calculations of OH, HO_2 and RO_2 radicals, *Atmospheric chemistry and physics*, 17, 663-690, 2017.
- 749 Tao, J., Zhang, L. M., Cao, J. J., and Zhang, R. J.: A review of current knowledge concerning $PM_{2.5}$
750 chemical composition, aerosol optical properties and their relationships across China, *Atmos. Chem.*
751 *Phys.*, 17, 9485-9518, 10.5194/acp-17-9485-2017, 2017.
- 752 Tao, Y., Ye, X., Ma, Z., Xie, Y., Wang, R., Chen, J., Yang, X., and Jiang, S.: Insights into different nitrate
753 formation mechanisms from seasonal variations of secondary inorganic aerosols in Shanghai, *Atmos.*
754 *Environ.*, 145, 1-9, 10.1016/j.atmosenv.2016.09.012, 2016.
- 755 Tian, J., Wang, Q., Zhang, Y., Yan, M., Liu, H., Zhang, N., Ran, W., and Cao, J.: Impacts of primary
756 emissions and secondary aerosol formation on air pollution in an urban area of China during the
757 COVID-19 lockdown, *Environ. Int.*, 150, 106426, 2021.
- 758 Trinh, H. T., Imanishi, K., Morikawa, T., Hagino, H., and Takenaka, N.: Gaseous nitrous acid (HONO)
759 and nitrogen oxides (NO_x) emission from gasoline and diesel vehicles under real-world driving test
760 cycles, *J. Air. Waste. Manage.*, 67, 412-420, 2017.
- 761 von Schneidemesser, E., Monks, P. S., Allan, J. D., Bruhwiler, L., Forster, P., Fowler, D., Lauer, A.,
762 Morgan, W. T., Paasonen, P., Righi, M., Sindelarova, K., and Sutton, M. A.: Chemistry and the
763 Linkages between Air Quality and Climate Change, *Chem. Rev.*, 115, 3856-3897,
764 10.1021/acs.chemrev.5b00089, 2015.



- 765 Wagner, N., Riedel, T., Young, C., Bahreini, R., Brock, C., Dubé, W., Kim, S., Middlebrook, A., Öztürk,
766 F., and Roberts, J.: N₂O₅ uptake coefficients and nocturnal NO₂ removal rates determined from
767 ambient wintertime measurements, *Journal of Geophysical Research: Atmospheres*, 118, 9331-9350,
768 2013.
- 769 Wang, H., Lu, K., Chen, X., Zhu, Q., Chen, Q., Guo, S., Jiang, M., Li, X., Shang, D., Tan, Z., Wu, Y.,
770 Wu, Z., Zou, Q., Zheng, Y., Zeng, L., Zhu, T., Hu, M., and Zhang, Y.: High N₂O₅ Concentrations
771 Observed in Urban Beijing: Implications of a Large Nitrate Formation Pathway, *Environ. Sci.*
772 *Technol. Lett.*, 4, 416-420, 10.1021/acs.estlett.7b00341, 2017.
- 773 Wang, J., Li, J., Ye, J., Zhao, J., Wu, Y., Hu, J., Liu, D., Nie, D., Shen, F., Huang, X., Huang, D. D., Ji,
774 D., Sun, X., Xu, W., Guo, J., Song, S., Qin, Y., Liu, P., Turner, J. R., Lee, H. C., Hwang, S., Liao, H.,
775 Martin, S. T., Zhang, Q., Chen, M., Sun, Y., Ge, X., and Jacob, D. J.: Fast sulfate formation from
776 oxidation of SO₂ by NO₂ and HONO observed in Beijing haze, *Nat. Commun.*, 11, 2844,
777 10.1038/s41467-020-16683-x, 2020a.
- 778 Wang, W., Yu, J., Cui, Y., He, J., Xue, P., Cao, W., Ying, H., Gao, W., Yan, Y., Hu, B., Xin, J., Wang, L.,
779 Liu, Z., Sun, Y., Ji, D., and Wang, Y.: Characteristics of fine particulate matter and its sources in an
780 industrialized coastal city, Ningbo, Yangtze River Delta, China, *Atmos. Res.*, 203, 105-117,
781 10.1016/j.atmosres.2017.11.033, 2018.
- 782 Wang, Y., Zhang, R., and Saravanan, R.: Asian pollution climatically modulates mid-latitude cyclones
783 following hierarchical modelling and observational analysis, *Nature communications*, 5, 1-7, 2014.
- 784 Wang, Y., Chen, Y., Wu, Z., Shang, D., Bian, Y., Du, Z., Schmitt, S. H., Su, R., Gkatzelis, G. I., Schlag,
785 P., Hohaus, T., Voliotis, A., Lu, K., Zeng, L., Zhao, C., Alfarra, M. R., McFiggans, G., Wiedensohler,
786 A., Kiendler-Scharr, A., Zhang, Y., and Hu, M.: Mutual promotion between aerosol particle liquid
787 water and particulate nitrate enhancement leads to severe nitrate-dominated particulate matter
788 pollution and low visibility, *Atmos. Chem. Phys.*, 20, 2161-2175, 10.5194/acp-20-2161-2020, 2020b.
- 789 Wayne, R. P., Barnes, I., Biggs, P., Burrows, J., Canosa-Mas, C., Hjorth, J., Le Bras, G., Moortgat, G.,
790 Perner, D., and Poulet, G.: The nitrate radical: Physics, chemistry, and the atmosphere, *Atmospheric*
791 *Environment. Part A. General Topics*, 25, 1-203, 1991.
- 792 Wen, L., Xue, L., Wang, X., Xu, C., Chen, T., Yang, L., Wang, T., Zhang, Q., and Wang, W.: Summertime
793 fine particulate nitrate pollution in the North China Plain: increasing trends, formation mechanisms
794 and implications for control policy, *Atmos. Chem. Phys.*, 18, 11261-11275, 10.5194/acp-18-11261-
795 2018, 2018.
- 796 Wen, L., Chen, J., Yang, L., Wang, X., Xu, C., Sui, X., Yao, L., Zhu, Y., Zhang, J., and Zhu, T.: Enhanced
797 formation of fine particulate nitrate at a rural site on the North China Plain in summer: The important
798 roles of ammonia and ozone, *Atmos. Environ.*, 101, 294-302, 2015.
- 799 Wolfe, G. M., Marvin, M. R., Roberts, S. J., Travis, K. R., and Liao, J.: The framework for 0-D
800 atmospheric modeling (FOAM) v3.1, *Geoscientific Model Development*, 9, 3309-3319, 2016.
- 801 Wong, K., Oh, H.-J., Lefer, B., Rappenglück, B., and Stutz, J.: Vertical profiles of nitrous acid in the
802 nocturnal urban atmosphere of Houston, TX, *Atmos. Chem. Phys.*, 11, 3595-3609, 2011.
- 803 Wong, K., Tsai, C., Lefer, B., Grossberg, N., and Stutz, J.: Modeling of daytime HONO vertical gradients
804 during SHARP 2009, *Atmos. Chem. Phys.*, 13, 3587-3601, 2013.
- 805 Xie, Y., Ding, A., Nie, W., Mao, H., Qi, X., Huang, X., Xu, Z., Kerminen, V. M., Petäjä, T., and Chi, X.:
806 Enhanced sulfate formation by nitrogen dioxide: Implications from in situ observations at the
807 SORPES station, *J. Geophys. Res.-Atmos.*, 120, 12679-12694, 2015.
- 808 Xie, Y., Wang, G., Wang, X., Chen, J., Chen, Y., Tang, G., Wang, L., Ge, S., Xue, G., Wang, Y., and Gao,
809 J.: Nitrate-dominated PM_{2.5} and elevation of particle pH observed in urban Beijing during the winter
810 of 2017, *Atmos. Chem. Phys.*, 20, 5019-5033, 10.5194/acp-20-5019-2020, 2020.
- 811 Xu, Q., Wang, S., Jiang, J., Bhattarai, N., Li, X., Chang, X., Qiu, X., Zheng, M., Hua, Y., and Hao, J.:
812 Nitrate dominates the chemical composition of PM_{2.5} during haze event in Beijing, China, *Sci. Total*
813 *Environ.*, 689, 1293-1303, 2019.
- 814 Xue, C., Zhang, C., Ye, C., Liu, P., Catoire, V., Krysztofiak, G., Chen, H., Ren, Y., Zhao, X., Wang, J.,
815 Zhang, F., Zhang, C., Zhang, J., An, J., Wang, T., Chen, J., Kleffmann, J., Mellouki, A., and Mu, Y.:
816 HONO Budget and Its Role in Nitrate Formation in the Rural North China Plain, *Environ. Sci.*
817 *Technol.*, 54, 11048-11057, 10.1021/acs.est.0c01832, 2020.
- 818 Yang, G., Liu, Y., and Li, X.: Spatiotemporal distribution of ground-level ozone in China at a city level,
819 *Sci. Rep.*, 10, 1-12, 2020.
- 820 Ye, C., Zhou, X., Pu, D., Stutz, J., Festa, J., Spolaor, M., Tsai, C., Cantrell, C., Mauldin, R. L., and
821 Campos, T.: Rapid cycling of reactive nitrogen in the marine boundary layer, *Nature*, 532, 489-491,
822 2016.



- 823 Ye, S., Ma, T., Duan, F., Li, H., He, K., Xia, J., Yang, S., Zhu, L., Ma, Y., and Huang, T.: Characteristics
824 and formation mechanisms of winter haze in Changzhou, a highly polluted industrial city in the
825 Yangtze River Delta, China, *Environ. Pollut.*, 253, 377-383, 2019.
- 826 Ye, Z., Liu, J., Gu, A., Feng, F., Liu, Y., Bi, C., Xu, J., Li, L., Chen, H., Chen, Y., Dai, L., Zhou, Q., and
827 Ge, X.: Chemical characterization of fine particulate matter in Changzhou, China, and source
828 apportionment with offline aerosol mass spectrometry, *Atmos. Chem. Phys.*, 17, 2573-2592,
829 10.5194/acp-17-2573-2017, 2017.
- 830 Yu, C., Wang, Z., Xia, M., Fu, X., Wang, W., Tham, Y. J., Chen, T., Zheng, P., Li, H., Shan, Y., Wang, X.,
831 Xue, L., Zhou, Y., Yue, D., Ou, Y., Gao, J., Lu, K., Brown, S. S., Zhang, Y., and Wang, T.:
832 Heterogeneous N_2O_5 reactions on atmospheric aerosols at four Chinese sites: improving model
833 representation of uptake parameters, *Atmospheric Chemistry and Physics*, 20, 4367-4378,
834 10.5194/acp-20-4367-2020, 2020a.
- 835 Yu, Y., Xu, H., Jiang, Y., Chen, F., and Liu, D.: A modeling study of $PM_{2.5}$ transboundary transport during
836 a winter severe haze episode in southern Yangtze River Delta, China, *Atmos. Res.*, 248, 105159,
837 2020b.
- 838 Yun, H., Wang, W., Wang, T., Xia, M., Yu, C., Wang, Z., Poon, S. C., Yue, D., and Zhou, Y.: Nitrate
839 formation from heterogeneous uptake of dinitrogen pentoxide during a severe winter haze in southern
840 China, *Atmos. Chem. Phys.*, 18, 17515-17527, 2018.
- 841 Zare, A., Romer, P. S., Nguyen, T., Keutsch, F. N., Skog, K., and Cohen, R. C.: A comprehensive organic
842 nitrate chemistry: insights into the lifetime of atmospheric organic nitrates, *Atmos. Chem. Phys.*, 18,
843 15419-15436, 10.5194/acp-18-15419-2018, 2018.
- 844 Zhai, S., Jacob, D. J., Wang, X., Liu, Z., Wen, T., Shah, V., Li, K., Moch, J. M., Bates, K. H., Song, S.,
845 Shen, L., Zhang, Y., Luo, G., Yu, F., Sun, Y., Wang, L., Qi, M., Tao, J., Gui, K., Xu, H., Zhang, Q.,
846 Zhao, T., Wang, Y., Lee, H. C., Choi, H., and Liao, H.: Control of particulate nitrate air pollution in
847 China, *Nat. Geosci.*, 14, 389-395, 10.1038/s41561-021-00726-z, 2021.
- 848 Zhang, Q., Zheng, Y. X., Tong, D., Shao, M., Wang, S. X., Zhang, Y. H., Xu, X. D., Wang, J. N., He, H.,
849 Liu, W. Q., Ding, Y. H., Lei, Y., Li, J. H., Wang, Z. F., Zhang, X. Y., Wang, Y. S., Cheng, J., Liu, Y.,
850 Shi, Q. R., Yan, L., Geng, G. N., Hong, C. P., Li, M., Liu, F., Zheng, B., Cao, J. J., Ding, A. J., Gao,
851 J., Fu, Q. Y., Huo, J. T., Liu, B. X., Liu, Z. R., Yang, F. M., He, K. B., and Hao, J. M.: Drivers of
852 improved $PM_{2.5}$ air quality in China from 2013 to 2017, *Proc. Natl. Acad. Sci. U.S.A.*, 116, 24463-
853 24469, 10.1073/pnas.1907956116, 2019.
- 854 Zhang, T., Shen, Z., Su, H., Liu, S., Zhou, J., Zhao, Z., Wang, Q., Prévôt, A., and Cao, J.: Effects of
855 Aerosol Water Content on the formation of secondary inorganic aerosol during a Winter Heavy $PM_{2.5}$
856 Pollution Episode in Xi'an, China, *Atmos. Environ.*, 252, 118304, 2021.
- 857 Zhang, Y.-L. and Cao, F.: Fine particulate matter ($PM_{2.5}$) in China at a city level, *Sci. Rep.*, 5, 1-12, 2015.
- 858 Zhao, P., Dong, F., He, D., Zhao, X., Zhang, X., Zhang, W., Yao, Q., and Liu, H.: Characteristics of
859 concentrations and chemical compositions for $PM_{2.5}$ in the region of Beijing, Tianjin, and Hebei,
860 China, *Atmos. Chem. Phys.*, 13, 4631-4644, 2013.
- 861 Zhao, Q., Huo, J., Yang, X., Fu, Q., Duan, Y., Liu, Y., Lin, Y., and Zhang, Q.: Chemical characterization
862 and source identification of submicron aerosols from a year-long real-time observation at a rural site
863 of Shanghai using an Aerosol Chemical Speciation Monitor, *Atmos. Res.*, 246,
864 10.1016/j.atmosres.2020.105154, 2020a.
- 865 Zhao, Y. B., Zhang, K., Xu, X. T., Shen, H. Z., Zhu, X., Zhang, Y. X., Hu, Y. T., and Shen, G. F.:
866 Substantial Changes in Nitrogen Dioxide and Ozone after Excluding Meteorological Impacts during
867 the COVID-19 Outbreak in Mainland China, *Environ. Sci. Technol. Lett.*, 7, 402-408, 2020b.
- 868 Zheng, B., Tong, D., Li, M., Liu, F., Hong, C. P., Geng, G. N., Li, H. Y., Li, X., Peng, L. Q., Qi, J., Yan,
869 L., Zhang, Y. X., Zhao, H. Y., Zheng, Y. X., He, K. B., and Zhang, Q.: Trends in China's
870 anthropogenic emissions since 2010 as the consequence of clean air actions, *Atmos. Chem. Phys.*,
871 18, 14095-14111, 10.5194/acp-18-14095-2018, 2018.
- 872 Zheng, H., Kong, S., Chen, N., Yan, Y., Liu, D., Zhu, B., Xu, K., Cao, W., Ding, Q., Lan, B., Zhang, Z.,
873 Zheng, M., Fan, Z., Cheng, Y., Zheng, S., Yao, L., Bai, Y., Zhao, T., and Qi, S.: Significant changes
874 in the chemical compositions and sources of $PM_{2.5}$ in Wuhan since the city lockdown as COVID-19,
875 *Sci. Total. Environ.*, 739, 140000, 10.1016/j.scitotenv.2020.140000, 2020.
- 876 Zhong, H., Huang, R.-J., Chang, Y., Duan, J., Lin, C., and Chen, Y.: Enhanced formation of secondary
877 organic aerosol from photochemical oxidation during the COVID-19 lockdown in a background site
878 in Northwest China, *Sci. Total. Environ.*, 778, 144947, 2021.

879

880



881 Table 1 Parameterization of the formation and removal pathways of HONO added to the model.

Mechanism	Parametrization	Max	Min	Ref
NO ₂ +aerosol→0.5HONO+0.5HNO ₃	$\gamma\text{NO}_2=2\times 10^{-6}$	1×10 ⁻⁵	4×10 ⁻⁷	a-d
NO ₂ +ground→HONO	$\gamma\text{NO}_2=2\times 10^{-6}$	1×10 ⁻⁵	4×10 ⁻⁷	a-d
NO ₂ +aerosol+hv→HONO	$\gamma\text{NO}_2=2\times 10^{-5}\times j\text{NO}_2/j\text{NO}_2\text{noon}^*$	1×10 ⁻⁴	4×10 ⁻⁶	b, e-g
NO ₂ +ground+hv→HONO	$\gamma\text{NO}_2=2\times 10^{-5}\times j\text{NO}_2/j\text{NO}_2\text{noon}^*$	1×10 ⁻⁴	4×10 ⁻⁶	b, e-g
pNO ₃ +hv→HONO	$j\text{NO}_3= j\text{HNO}_3\times 30$	100	1	h, i
Vehicular emission	HONO/NO _x =0.8%	0.18%	1.6%	j-l
NO ₂ +SO ₂ +aerosol→HONO+SO ₄ ²⁻	$k_{aq}=1.4\times 10^5\text{ M}^{-1}\text{ s}^{-1}$ (pH < 5); $2\times 10^6\text{ M}^{-1}\text{ s}^{-1}$ (pH > 6)			m, n
HONO deposition	$k_{dep}=\exp^{(23920/T-91.5)}/\text{PBL}$			a

882 *The value of $j\text{NO}_2\text{noon}$ used in the model was 0.005 s⁻¹; References: ^aXue et al. (2020); ^bLiu et al.
 883 (2019); ^cWong et al. (2011); ^dKleffmann et al. (1998); ^eWong et al. (2013); ^fZare et al. (2018); ^gHan
 884 et al. (2016); ^hRomer et al. (2018); ⁱYe et al. (2016); ^jKurtenbach et al. (2001); ^kLiu et al. (2017),
 885 ^lTrinh et al. (2017); ^mLee and Schwartz (1983); ⁿWang et al. (2020a).

886

887

888

889 Table 2 Concentrations (average ± standard deviation) of PM_{2.5}, particulate nitrate, NO_x, and O₃, as
 890 well as temperature and RH at Qingpu and Pudong sites in the winter of 2018 and 2019.

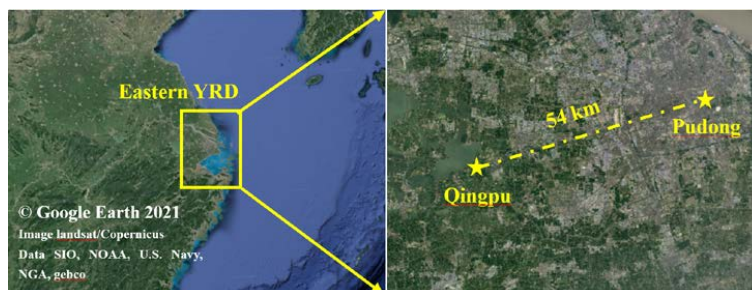
	Sites			
	Qingpu-2018	Pudong-2018	Qingpu-2019	Pudong-2019
PM _{2.5} (μg m ⁻³)	50.0 ± 34.8	40.9 ± 32.5	58.6 ± 37.2	49.5 ± 35.3
NO ₃ ⁻ (μg m ⁻³)	14.9 ± 12.8	11.9 ± 12.2	17.0 ± 14.8	13.2 ± 12.0
NO _x (ppb)	29.6 ± 31.1	27.5 ± 24.4	35.1 ± 33.1	26.9 ± 21.3
O ₃ (ppb)	19.1 ± 12.7	18.8 ± 10.4	21.7 ± 14.3	22.3 ± 12.0
Temperature (°C)	6.6 ± 4.4	7.3 ± 4.2	7.5 ± 4.2	8.2 ± 3.8
RH (%)	80 ± 17	78 ± 18	80 ± 17	79 ± 20

891

892



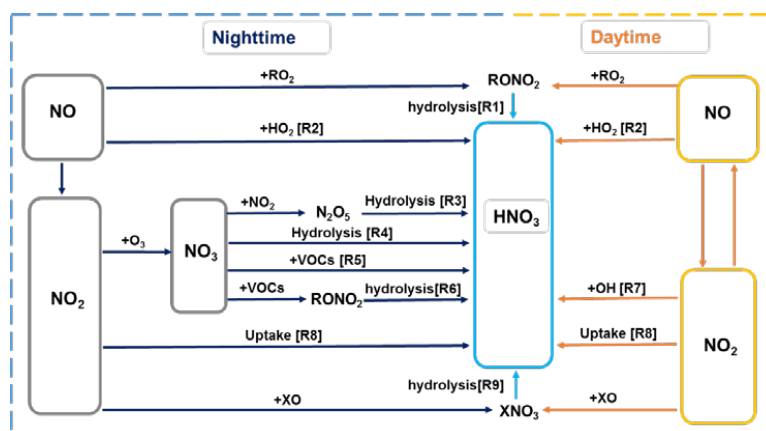
893



894

895 Figure 1 Map of the eastern YRD region and the two observation sites, i.e., Qingpu (suburban and
896 regional) and Pudong (urban).

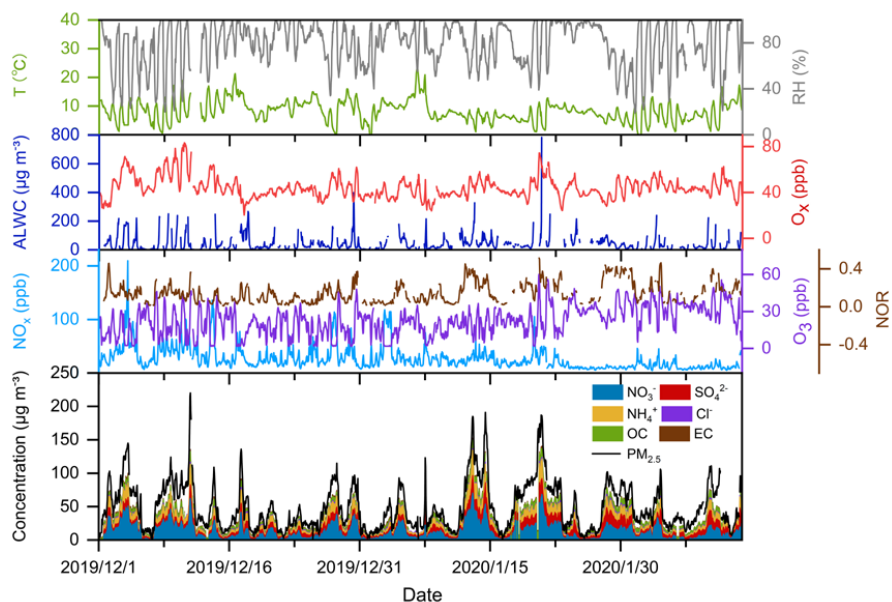
897



898

899 Figure 2 Simplified HNO₃ formation mechanisms in the troposphere. X represents Cl, Br, and I.

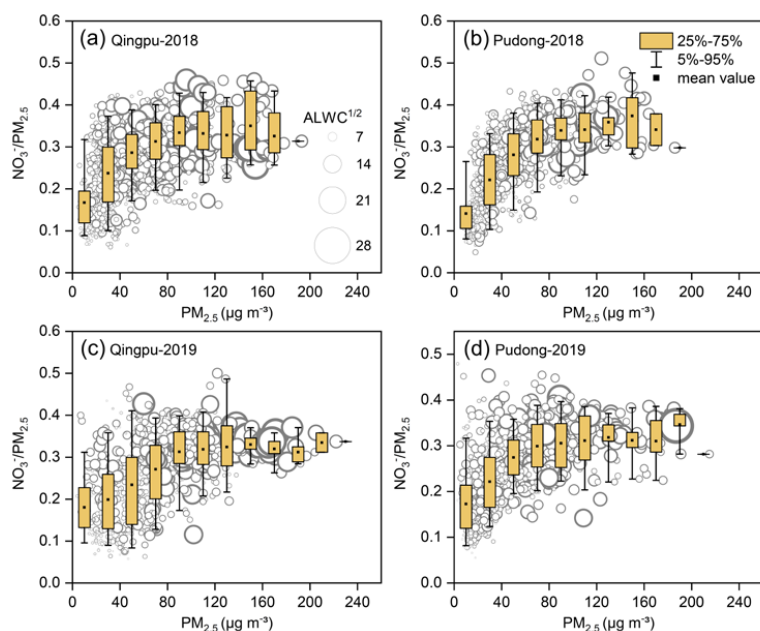
900



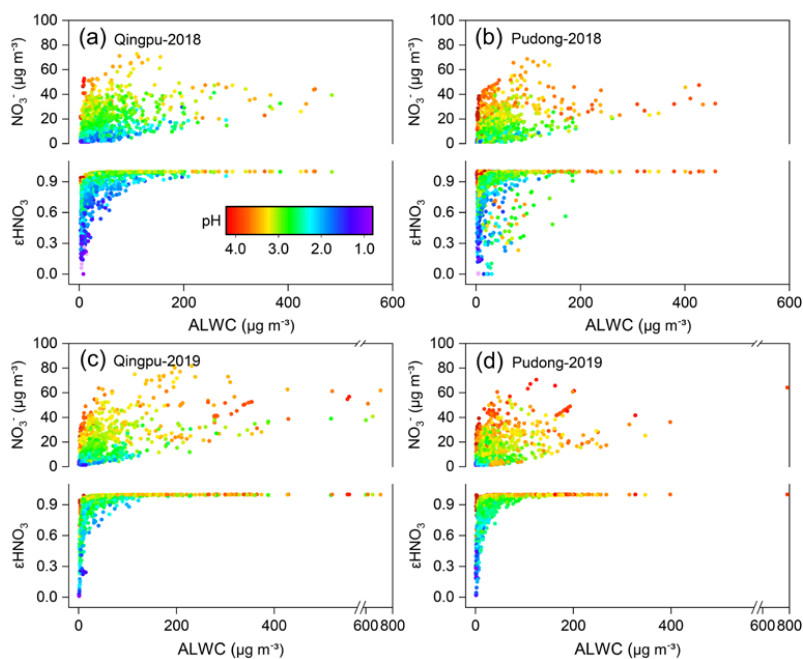
901

902 Figure 3 Time series of temperature, relative humidity (RH), aerosol liquid water content (ALWC),
903 NO_x , O_3 , O_x , nitrogen oxidation ratio (NOR), as well as $\text{PM}_{2.5}$ and major particulate compositions
904 at the Pudong site in the winter of 2019.

905



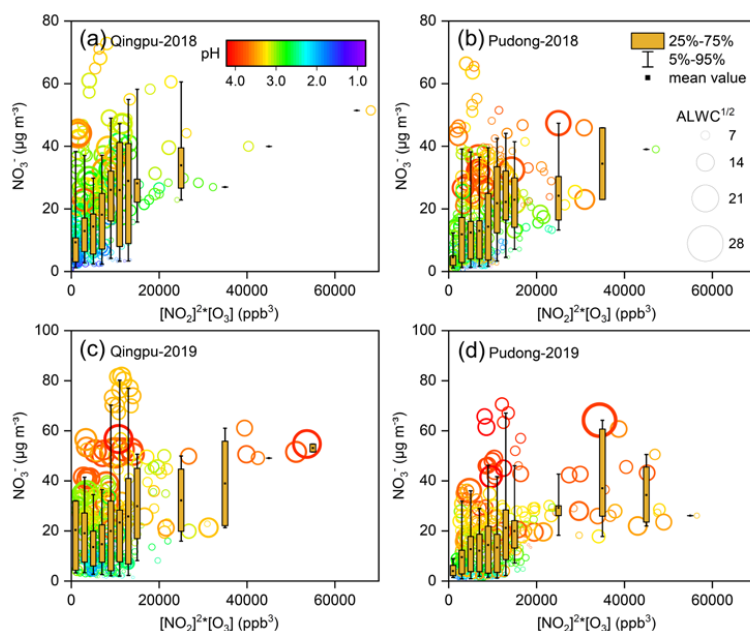
906
907 Figure 4 Mass ratio of nitrate to $\text{PM}_{2.5}$ as a function of $\text{PM}_{2.5}$ concentration at (a, c) Qingpu and (b,
908 d) Pudong sites in the winter of 2018 and 2019. The circles represent the measured ratio of NO_3^-
909 $/\text{PM}_{2.5}$, and their area is linearly scaled with square root of ALWC.
910



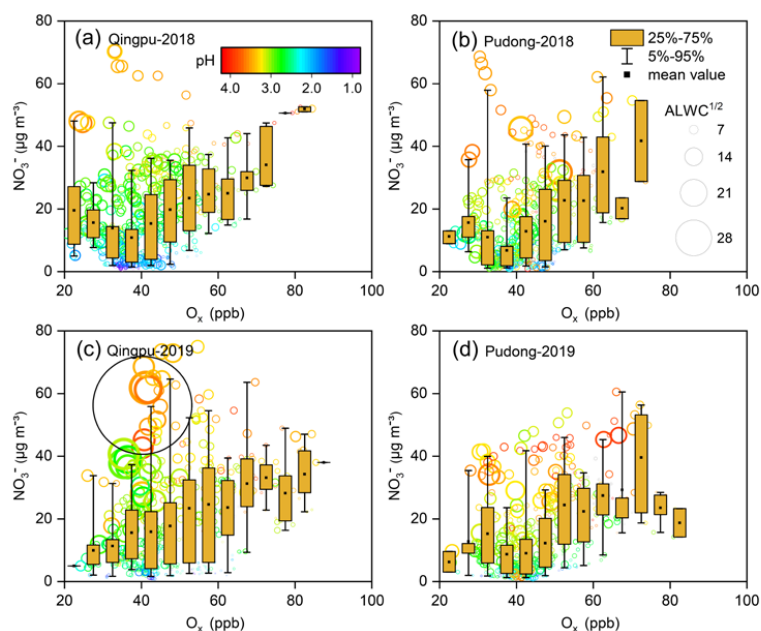
911

912 Figure 5 Particulate nitrate concentration and its fraction to total nitrate (ϵHNO_3) as a function of
913 ALWC and aerosol pH at (a, c) Qingpu and (b, d) Pudong sites in the winter of 2018 and 2019. The
914 circles are colored according to aerosol pH.

915



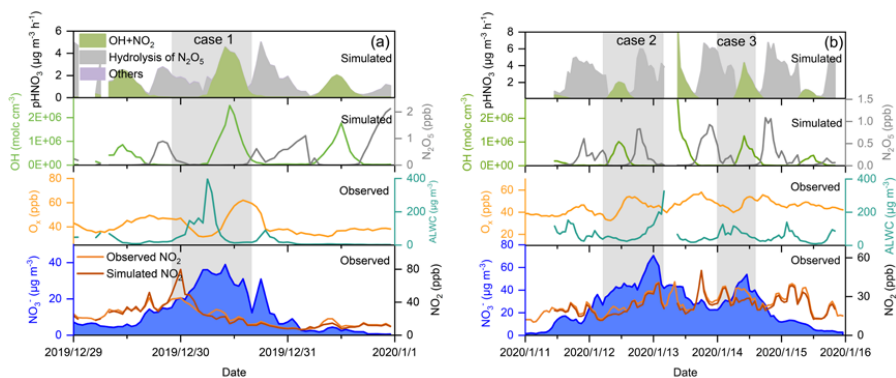
916
917 Figure 6 Particulate nitrate concentration as a function of $[\text{NO}_2]^2 \times [\text{O}_3]$ during the nighttime at (a, c)
918 Qingpu and (b, d) Pudong sites in 2018 and 2019. The circles are colored according to aerosol pH
919 and their size is linearly scaled with square root of ALWC.
920



921

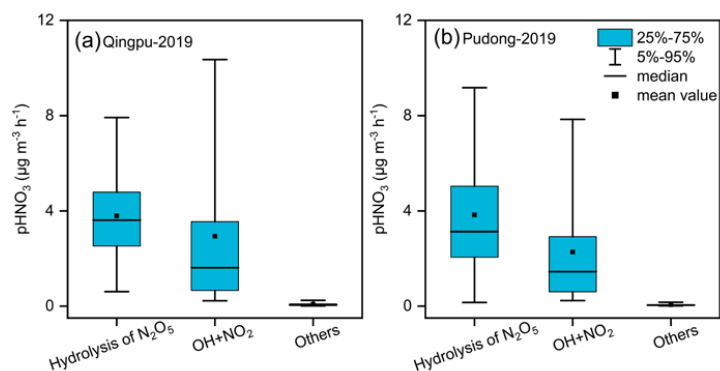
922 Figure 7 Particulate nitrate concentration as a function of O_x during the daytime at (a, c) Qingpu
923 and (b, d) Pudong sites in 2018 and 2019. The circles are colored according to aerosol pH and their
924 size is linearly scaled with square root of ALWC. The data points inside the black circle in (c)
925 correspond to low O_x levels but high ALWC and nitrate concentrations.

926



927

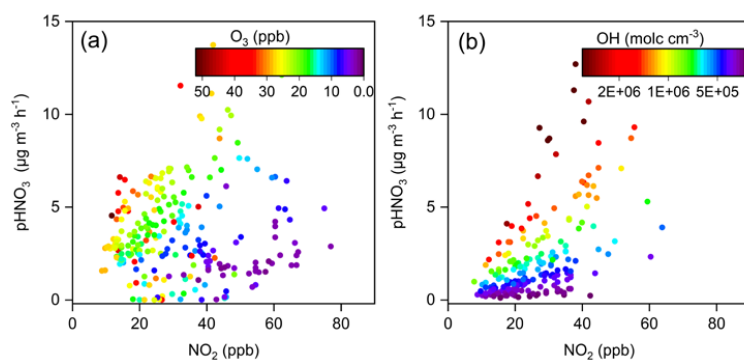
928 Figure 8 Time series of particulate nitrate, NO_2 , O_3 , ALWC, OH, N_2O_5 , as well as the formation rate
929 of HNO_3 from different processes during the two selected case during the pollution episodes at the
930 Pudong site in 2019. The simulated data with $\text{RH} > 95\%$ were not included in the figure (see main
931 text).
932



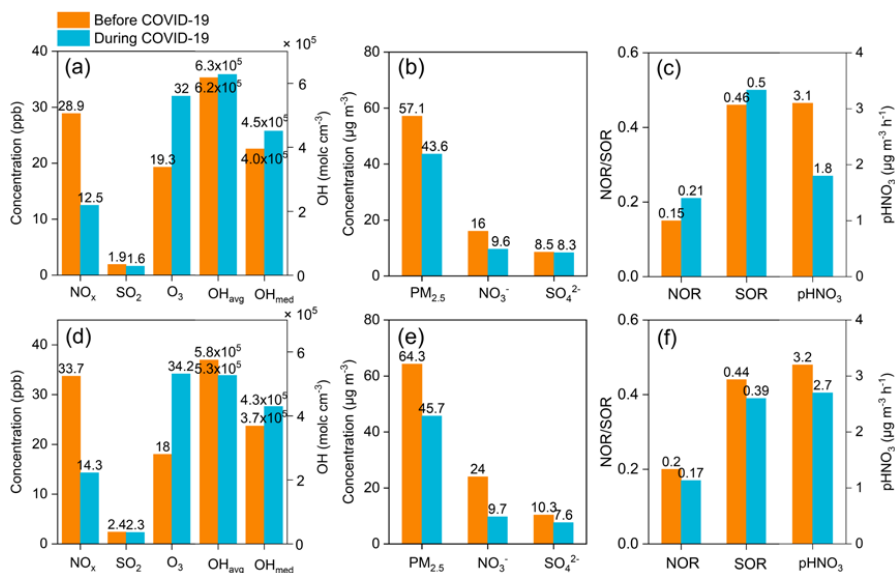
933

934 Figure 9 Simulated average formation rates of HNO₃ at (a) Qingpu and (b) Pudong sites during the
935 haze pollution periods in 2019

936



937
938 Figure 10 Production rates of HNO₃ from the (a) heterogeneous and (b) gas-phase processes as a
939 function of NO₂ concentration at the Pudong site during the nighttime and daytime, respectively.
940 The circles are colored according to the O₃ concentration in (a) and OH radical concentration in (b).
941



942

943 Figure 11 Average concentrations of NO_x, SO₂, O₃, OH radicals, PM_{2.5}, nitrate, sulfate, as well as
 944 the nitrogen and sulfur oxidation ratio (NOR and SOR) at (a-c) Pudong and (d-f) Qingpu sites before
 945 (1-22 January, 2020) and during (23 January-12 February, 2020) the COVID-19 epidemic.